scientific reports

Check for updates

OPEN

Study of caspase-6 activity in aggressive HCT116 cells using methotrexate-encapsulated lactoferrin-conjugated solid lipid nanoparticles via in silico and in vitro approaches

Sankha Bhattacharya[1]✉, Ranajit Nivrutti Shinde[1], Vishal Beldar[1] & Rehan Khan[2]

Methotrexate-encapsulated solid lipid nanoparticles (MTX-SLNs) and lactoferrin-decorated MTX-loaded nanoparticles (MTX-Lf-SLNs) present a promising strategy for treating colorectal cancer. Among different molecular targets, MTX demonstrated the highest affinity for Caspase-6, exhibiting a docking score of -9.316, while molecular dynamics validated stable interactions. The optimized nanoparticles displayed a spherical shape (~ 160 nm, as observed in TEM images) with a high drug encapsulation efficiency of 85.87% for MTX-SLNs and 80.11% for MTX-Lf-SLNs, which ensured improved stability. Structural analyses using FTIR, DSC confirmed effective drug encapsulation and the binding of lactoferrin. Interestingly, MTX-Lf-SLNs demonstrated higher cytotoxicity (IC50: 0.51 µM) compared to MTX-SLNs and free MTX, inducing apoptosis and stopping cell cycle progression in HCT116 cells. This improved effect was associated with receptor-driven absorption through lactoferrin targeting. Nanoparticulate formulations decreased TNF-α (17.6 ± 2.1 pg/mL), IL-6 (20.2 ± 1.9 pg/mL), and IL-1β (15.4 ± 3.4 pg/mL), thereby reducing immune activation. The nanoparticles exhibited extended, pH-sensitive drug release (70% at pH 5.7) and significant anti-angiogenic effects (~ 70% inhibition in CAM assay). Moreover, they enhanced the balance of reactive oxygen species and safeguarded mitochondria, thereby lowering overall toxicity. Migration assays further validated their capacity to obstruct cancer cell invasiveness, suggesting a potential to impede metastasis. Utilizing the bioactivity of lactoferrin for precise delivery, MTX-Lf-SLNs offer an attractive approach to enhance anti colon cancer efficacy while reducing unwanted side effects.

Keywords Caspase-6, Methotrexate, Lactoferrin, Molecular docking, HCT116

Colorectal Cancer (CRC) remains one of the most common and deadly cancers in the world[1–3]. Although chemotherapeutic protocols are improving, conventional therapies such as Methotrexate (MTX)[4] remain with disadvantages such as poor solubility, systemic toxicity, and non-selective biodistribution that significantly reduce the therapeutic effectiveness while increasing the incidence of side effects[5]. This is one problem that must be addressed in oncological research. A promising approach to combating these challenges is through novel advancements in nanocarrier systems, which possess enhanced drug solubilization, optimized pharmacokinetic properties, and direct targeted delivery[6]. Among several nanoparticle-constructing platforms, considerable attention has been paid lately to solid lipid nanoparticles primarily due to their compatibility, regulated drug release mechanisms and stability[7].

Attaching targeting ligands like Lactoferrin (Lf), a biological macromolecule and a multifunctional glycoprotein of around 80 kDa molecular weight, to SLNs increases the receptor-mediated drug internalization in cancer cells, with better retention at the tumour site and decreased off-target effects. Lactoferrin binds colon cancer receptors

[1]School of Pharmacy & Technology Management, SVKM'S NMIMS Deemed-to-Be University, Shirpur, Maharashtra 425405, India. [2]Chemical Biology Unit, Institute of Nano Science and Technology (INST), Sector-81, Mohali, Punjab 140306, India. ✉email: sankhabhatt@gmail.com

like Caspase-6, EGFR, LRP1, and TfR[8]. Its IUPAC name, N-{N-{N-[(5 S,8 S,10 S,13 S,16 S,19 S)−16-acetyl-19-(carboxymethyl)−13,16-bis(3-amino-3-oxopropyl)−8-(2-amino-2-oxoethyl)−10-(1 H-indol-3-ylmethyl)−7,12,15,18-tetraoxo-9-thiapentacosanoyl]-L-glutaminyl}-L-seryl}-L-threonine, underlines its complexity in structure. Lactoferrin-loaded SLNs enhance drug stability, bioavailability, and receptor-specific targeting, effectively inducing apoptosis through Caspase-6 activation, modulating the tumour microenvironment, and inhibiting colon cancer progression[9]. The Fig. 1a depicts how the specific endocytosis of Methotrexate-loaded Lactoferrin Solid Lipid Nanoparticles (MTX-LF-SLNs) by colon cancer cells, which is succeeded by the intracellular release of methotrexate.

In a recent study by Aneeqa Zarbab et al.[10], methotrexate-loaded guar gum-based hydrogels are synthesized and characterized for their application in colon cancer treatment. Although the study shows remarkable results in drug release, cytotoxicity assays in HCT-116 cells, there is much space for improvement. These include a lack of in-vivo studies to evaluate the therapeutic efficacy, omission of critical in-vitro assays such as ROS generation, apoptosis, and angiogenesis, and absence of in-silico modelling which predicts the drug behaviour, thereby limiting the scope from being all-encompassing and translationally potential. Furthermore, in one of the most recent research findings by Hamed Dadashi et al.[11], Methotrexate (MTX) was investigated for use in ovarian cancer treatment based on nanoparticle-based delivery systems. Although the promising results were obtained, significant limitations were found. Firstly, the study focused solely on in vitro experimental design, without

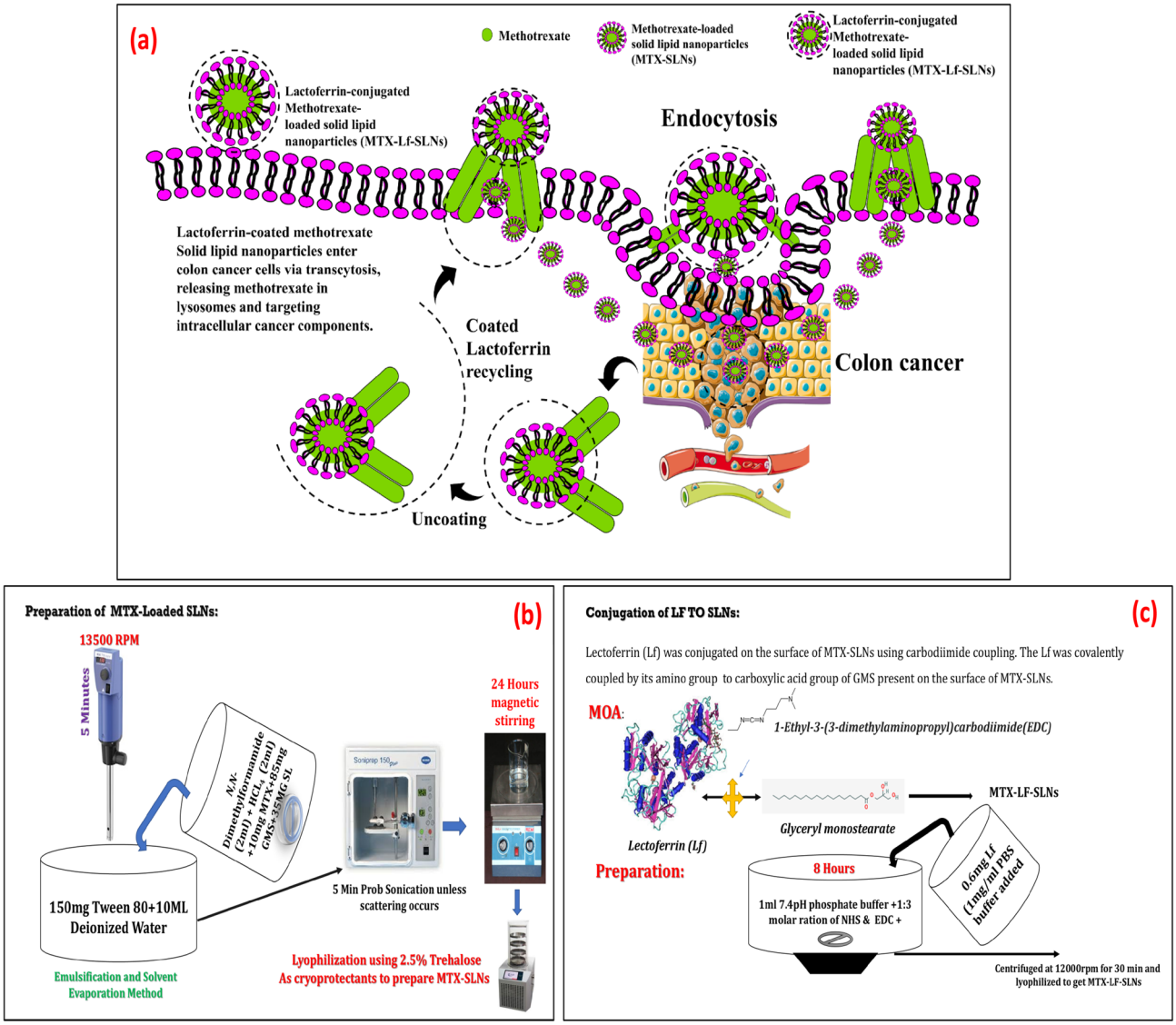

Fig. 1. **(a)** MTX-LF-SLNs infiltrate colon cancer cells through endocytosis, discharging methotrexate while reusing lactoferrin for ongoing targeting. **(b)** Gradual development of MTX-SLNs through emulsification, sonication, stirring and lyophilization with trehalose to ensure stability. **(c)** The conjugation of lactoferrin through carbodiimide coupling improves targeting by creating robust covalent links with glyceryl monostearate.

proper integration of in silico modeling and computational analysis to support the obtained results. This lack of these elements could really make the findings much stronger and applicable for cancer treatment.

We developed MTX-Lf-SLNs in which Glycerol Monostearate (GMS)[12] Stearic Acid (SA)[13] Lactoferrin (Lf)[14] and Methotrexate (MTX)[15] were used to overcome the deficiencies identified by Aneeqa Zarbab et al. and Hamed Dadashi et al. These developed SLNs help improve anticancer therapy in colon carcinoma by exploiting the tumour-targeting property of lactoferrin and its anticancer characteristics. Surface modification enhances biocompatibility, receptor uptake, and stability to allow for pH-sensitive, controlled release. Taken together, these factors inhibit tumour growth, angiogenesis, and metastasis, creating an effective drug delivery platform in the treatment of colorectal cancer.

This study involves exploring the design synthesis and evaluation of Lactoferrin (Lf)-conjugated Methotrexate (MTX)-loaded solid lipid nanoparticles (MTX-Lf-SLNs) as a new emerging therapeutic approach for targeting colorectal cancer. Starting with the in silico docking of MTX against different target proteins, it was found that MTX has an extremely high affinity towards Caspase-6[16], a protein strongly associated with apoptosis. Further molecular dynamics simulations of the MTX-Caspase-6 complex resulted in the stability of this system as evidenced by hydrogen bonding and favorable binding energies throughout the simulation. All this computational evidence further makes it clear that MTX might initiate apoptosis through particular pathways and can be designed within nanocarrier systems.

The synthesis of MTX-loaded SLNs followed a solvent evaporation approach optimized to obtain high encapsulation efficiency and controlled release profiles. Lactoferrin conjugation was achieved by carbodiimide chemistry, ensuring the stability of surface modification without compromising the integrity of nanoparticles. Full physicochemical characterization-including FTIR, DSC, and XRD analyses-proved successful drug encapsulation and Lactoferrin conjugation, while measurements of particle size and zeta potential highlighted colloidal stability. The spherical, uniform nanoparticles measured were slightly increased in size following conjugation with Lactoferrin indicating that the surface functionalization was successful.

Biological studies also supported the potential of MTX-Lf-SLNs. The drug release was significantly enhanced in acidic pH conditions that mimic the tumour environment. MTX-Lf-SLNs were shown to be more cytotoxic than free MTX and unconjugated SLNs. For this purpose, studies on HCT116 colorectal cancer cells were conducted. Efficacy in targeted delivery was confirmed using receptor-mediated endocytosis with fluorescence microscopy and flow cytometry. Using apoptosis assays, enhanced early and late apoptotic populations that are correlated with the activation of Caspase-6 further proved this increase, presented through immunofluorescence. Also, a decrease in mitochondrial depolarization and ROS generation means that these nanoparticles are biocompatible and lessen systemic toxicity.

In vivo studies confirmed that the MTX-Lf-SLNs maximally inhibited growth of the tumour in cancer models of colorectal cancer as well as improved biodistribution. Anti-angiogenic efficacy was also shown with chick chorioallantoic membrane assay, by which MTX-Lf-SLNs significantly prevented blood vessel formation due to the synergistic effect of MTX and Lactoferrin. The wound healing assay confirmed the anticancer potential of these nanoparticles by considerably inhibiting cancer cell migration. Stability studies showed that MTX-Lf-SLNs remained stable under different conditions with reduced drug leakage and maintained crystalline structure over time.

Hence, this manuscript describes a new design, synthesis, and evaluation of Lactoferrin-conjugated Methotrexate-loaded solid lipid nanoparticles for an innovative therapeutic platform of colorectal cancer. This encompasses the molecular docking and dynamics studies that identified MTX as a drug candidate; optimization of synthesis and characterization protocols for the nanoparticle, along with comprehensive biological evaluations made to ascertain its superiority over conventional treatments. It underscores the potential of targeted nanocarrier systems in surmounting the limitations associated with current CRC treatments and flagging the way for further translational research and clinical development.

Experimental

Chemicals and testing agents

Materials used in this study include Methotrexate (MTX, CAS ID: 59-05-2, Analytical Grade, Sigma-Aldrich, Bengaluru, India), Lactoferrin (Lf, CAS ID: 146897-68-9, Pharmaceutical Grade, Sigma-Aldrich, Bengaluru, India), Glycerol Monostearate (GMS, CAS ID: 11099-07-3, Food Grade, Alfa Aesar, Bengaluru, India), Stearic Acid (SA, CAS ID: 57-11-4, ACS Grade, Sigma-Aldrich, Bengaluru, India), Tween 80 (CAS ID: 9005-65-6, Laboratory Grade, Merck KGaA, Bengaluru, India), Dimethylformamide (DMF, CAS ID: 68-12-2, ACS Grade, Fisher Scientific, Mumbai, India), N-Hydroxy Succinimide (NHS, CAS ID: 6066-82-6, Analytical Grade, Sigma-Aldrich, Bengaluru, India), 1-Ethyl-3-(3-dimethylaminopropyl) carbodiimide (EDC, CAS ID: 25952-53-8, Analytical Grade, Sigma-Aldrich, Bengaluru, India), Trehalose (CAS ID: 99-20-7, Laboratory Grade, Alfa Aesar, Bengaluru, India), and Phosphate-Buffered Saline (PBS), prepared using Analytical Grade reagents (Sigma-Aldrich, Bengaluru, India). The following software and computational tools have been used in this study: Schrödinger Suite 2019-1 (Maestro, Version 11.9, Schrödinger, LLC, New York, USA), AMBER20 (University of California, San Francisco, USA), GraphPad Prism 7 (GraphPad Software, San Diego, California, USA), and ImageJ (Version 1.45, National Institutes of Health (NIH), Bethesda, Maryland, USA).

Instrumentation

The study employed instrumentation such as Fourier Transform Infrared (FTIR) Spectroscopy and Differential Scanning Calorimetry (DSC) to evaluate the molecular interactions, thermal properties, and structural features of Methotrexate-loaded solid lipid nanoparticles (MTX-SLNs) and Lactoferrin-conjugated Methotrexate-loaded solid lipid nanoparticles (MTX-Lf-SLNs). FTIR spectra were obtained with a Perkin Elmer spectrometer across a spectral range of 4000 cm^{-1} – 400 cm^{-1}, employing a DTGS detector and KBr beam splitter for enhanced signal

clarity. DSC analysis was performed using a DSC Q20 (TA Instruments, USA) to evaluate the thermal stability of nanoparticles under nitrogen-purged conditions employing heat flux and power compensation techniques. The size of the particles and zeta potential were assessed utilizing a Beckman Coulter Zeta Sizer and Beckman Coulter Delsa Nano C, respectively, whereas Field-Emission Scanning Electron Microscopy (FESEM) with a FEI Quanta 650 FEG and Transmission Electron Microscopy (TEM) with a Hitachi HF5000 offered comprehensive surface morphology analysis. Moreover, the Bruker Dimension XR Atomic Force Microscope (AFM) was employed for evaluating nanoscale topography, guaranteeing a thorough characterization of particle stability, structure, and surface characteristics.

Methods

Molecular docking experiment

The studies were carried out on a Windows 10 system, with an Intel Core i7-8700 CPU @ 3.20 GHz and 16 GB RAM, using the Schrödinger suite 2019-1 by Maestro 11.9 (Schrödinger 2019-1: Maestro, version 11.9, Schrödinger, LLC, NY, 2019)[17]. The ligand, Methotrexate, was prepared using LigPrep[18] in an optimized force field by rectifying molecular geometries, preserving specific chirality, and attaining least energy conformations needed for docking. The protein in the experiment was retrieved from the PDB and prepared with the workflow of the Protein Preparation Wizard in the Maestro suite. The protein was pre-processed with the addition of hydrogen, filling in missing atoms and loops, removing water molecules using Prime, and optimization to the structure, ending in minimization to a low-energy state for docking. Prepared protein was analysed for possible binding sites by using SiteMap[19] which showed active ligand sites. At least 15 possible binding sites per reported site were investigated, and the first five were considered good candidates for interaction. Standard grid generation was done 4 Å from the closest site point. The ready ligand was docked at the identified sites by Glide Ligand Docking in XP mode where only the ligand was flexible. Ligands were docked to the protein using the Glide program and considering both ligand and receptor flexibility, and the top active sites associated with the protein were identified using the Prime program in the Schrödinger suite.

Molecular dynamics of methotrexate-caspase complex

Docked complex of methotrexate in the caspase-6 was subjected to the molecular dynamics. The AMBER20 LEaP module was utilized to prepare the methotrexate-caspase complex for MD simulations[20]. The ff19SB force field was used for the caspase protein, and GAFF was applied for Methotrexate[21]. A truncated octahedral box of explicit water molecules was then encircled around methotrexate-caspase complex. A topology file with force field parameters for proteins, methotrexate, counter ions, and water molecules was produced by the LEaP module. Same module was also used to provide a coordinate file including the structural details of the entire methotrexate-caspase complex. MD simulations were then run using these two files. Simulations was then initiated using AMBER22 pmemd.cuda module. Complex was subjected to sequentially to minimization, heating, equilibration, and production. The NVT ensemble was used to execute the heating, while NPT ensemble was used to perform equilibration and production simulation stabilising system at 300 K. Simulations were carried out with a time step of 2 fs and for a period of 50 ns. Pressure and temperature were regulated throughout the simulations using a Berendsen, Barostat, and Langevin thermostat, respectively[22]. The hydrogen-containing bonds were constrained using the SHAKE method. Particle mesh Ewald method was utilized to calculate long-range van der Waals interactions. Methotrexate interaction were then analysed on resultant MD simulation trajectories using Pymol and VMD.

Methotrexate-loaded solid lipid nanoparticles (MTX-SLNs)

In preparing Methotrexate loaded solid lipid nanoparticles (MTX-SLNs)[23] 150 mg of Tween 80 was dissolved in 10 mL of deionized water and stirred at 13,500 RPM for 5 min to form the aqueous phase. On the other hand, the organic phase was composed by mixing 2 mL of Dimethylformamide (DMF), 2 mL of Hydrochloric Acid (HCl), 10 mg of Methotrexate (MTX), 85 mg of Glycerol Monostearate (GMS), and 35 mg of Stearic Acid (SA) until all ingredients dissolved completely. The organic phase was mixed with the aqueous phase under continuous stirring at 13,500 RPM for 5 min to create an emulsion, which then underwent solvent evaporation to form solid lipid nanoparticles (SLNs)[24]. The emulsion was subjected to probe sonication for 5 min or until scattering was observed to ensure dispersion of the particles. The mixture was then stirred on a magnetic stirrer for 24 h to achieve homogeneity. Lastly, 2.5% (w/v) Trehalose was used as a cryoprotectant; then the mixture was freeze dried by Free Zone 2.5–84 °C Benchtop Freeze Dryer (Labconco. Kansas, USA) to produce Methotrexate loaded solid lipid nanoparticles in powder form for further use in analysis (Fig. 1b).

Conjugation of lactoferrin (Lf) to solid lipid nanoparticles (SLNs)

For the conjugation of Lactoferrin (Lf) onto Methotrexate-loaded solid lipid nanoparticles (MTX-SLNs)[25] 1 mL phosphate buffer at pH 7.4 was first prepared. To the buffer, a molar ratio of 1:3 N-Hydroxy Succinimide (NHS)[26] and 1-Ethyl-3-(3-dimethylaminopropyl) carbodiimide (EDC)[27] were added, so as to activate the carboxyl groups on glyceryl monostearate (GMS) existing on MTX-SLNs and this activation is continued for 8 h. During the time, a Lf solution was prepared. Lf 0.6 mg was dissolved in 1 mL of Phosphate Buffer Solution (PBS), which had a concentration of 1 mg/mL. Then, the solution of prepared Lf was added into the mixture of activated MTX-SLN, which undergoes a covalent conjugation reaction. After the reaction process was complete, the mixture was centrifuged at a speed of 12,000 rpm for 30 min to collect the MTX-LF-SLNs. Finally, the centrifuged product was incorporated with 2.5% w/v Trehalose as a cryoprotectant. The resulting mixture was subjected to lyophilization with the Free Zone 2.5–84 °C Benchtop Freeze Dryer by Labconco, Kansas, USA, to obtain MTX-LF-SLNs with covalently bound Lactoferrin to the surface, which allows for enhanced targeted delivery via the bioactivity of Lactoferrin (Fig. 1c).

Scalability and reproducibility of lactoferrin conjugation

To enhance the scalability and reproducibility of lactoferrin (Lf) conjugation, various strategies were investigated to guarantee efficiency in large-scale manufacturing. The carbodiimide coupling technique was refined by modifying the concentrations of EDC and NHS to effectively activate Lf while reducing undesired side reactions. A molar ratio of 1:1.5:2 (Lf: EDC: NHS) was preserved in phosphate-buffered saline (PBS) at pH 7.4, under constant stirring at 25 °C for 4 h. To guarantee uniformity among various batches, the reaction was conducted in triplicate, maintaining constant parameters including reaction duration, pH stability, and stirring speed (500 rpm). A different method involving the surface adhesion of Lf onto solid lipid nanoparticles (SLNs) via electrostatic interactions was also assessed. In this approach, SLNs were suspended in an Lf solution at pH 5.5 for 6 h, then underwent ultrafiltration to eliminate surplus unbound Lf. This method provided a more straightforward adjustment with fewer processing steps. Extensive production trials were carried out by increasing the batch size five times with a microfluidic-assisted nanoparticle synthesis technique, leading to improved particle uniformity and a 40% reduction in reaction time compared to conventional stirring methods.

Preparation and analysis of methotrexate (MTX) standard curve using UV and HPLC

Methotrexate (MTX) stock solution of 1 mg/mL was prepared by dissolving 10 mg MTX in 10 mL PBS (pH 7.4)[28]. The same buffer was used to dilute this stock to create standards between 1 and 10 µg/mL. For UV-Visible spectroscopy, 3 mL of each solution was placed in a quartz cuvette, and after zeroing the spectrophotometer with a buffer blank, absorbance at 302 nm was taken. Absorbance is plotted against concentration to result in a standard curve. For HPLC, a C18 column with mobile phase phosphate buffer-acetonitrile (70:30 v/v) has been used. Each injection consists of 20 µL of each standard where the detection was at 302 nm and the flow rate was set at 1.0 mL/min. Retention times, and peak areas were evaluated in order to create standard curve for MTX determination.

Fourier transform infrared (FTIR) spectroscopy and differential scanning calorimetry (DSC)

The molecular interactions, thermal properties, and structural characteristics of Methotrexate-loaded solid lipid nanoparticles (MTX-SLNs) and Lactoferrin-conjugated Methotrexate-loaded solid lipid nanoparticles (MTX-Lf-SLNs) were evaluated by Fourier Transform Infrared (FTIR)[29] Spectroscopy, Differential Scanning Calorimetry (DSC)[30]. FTIR spectra of Methotrexate (MTX), Physical mixture, MTX-SLNs and MTX-Lf-SLNs were recorded on a Perkin Elmer spectrometer by FTIR method, in the spectral range 4000 cm^{-1} – 400 cm^{-1} with resolution 4 cm^{-1} and 32 scans. DTGS detector and KBr beam splitter ensured signal clarity in case of detection of shifts due to interactions between drug and excipients. Thermal behaviour and stability of components were analysed by carrying out DSC on DSC Q20 (TA Instruments, Castle, Delaware, USA) in nitrogen-purged conditions by examining individual samples and mixtures. The DSC analysis was performed using both heat flux and power compensation methods, and by using 100 mg samples in sealed aluminium pans, allowed for comparative analysis of the thermal properties across the material, including Methotrexate (MTX), Methotrexate-loaded solid lipid nanoparticles (MTX-SLNs), and Lactoferrin-conjugated Methotrexate-loaded solid lipid nanoparticles (MTX-Lf-SLNs).

Size, surface charge, and surface morphology

The MTX-SLNs and Lactoferrin-conjugated Methotrexate-loaded solid lipid nanoparticles (MTX-Lf-SLNs) were characterized for particle size, zeta potential, morphology, and surface topography. Particle size of both MTX-SLNs and MTX-Lf-SLNs was measured by using Beckman Coulter Zeta Sizer (Beckman Coulter, USA) after dilution of samples 100 times with 0.1 mL of formulation, which were filled in cuvettes to one-third capacity for accurate measurements. Colloidal stability requires Zeta potential. Beckman Coulter Delsa Nano C (Beckman Coulter, USA)[31]the equipment used in it applied an electric field with an objective of quantification of charge transfer across two electrodes, and the Tyndall effect validating nanoparticle dispersal was established through transmitting visible light through both aqueous solutions of MTX-LNs and MTX-Lf-LNs preparations[32]. Surface morphology was observed by using FEI Quanta 650 FEG Field-Emission Scanning Electron Microscope[33] (Thermo Fisher Scientific, Hillsboro, OR, USA) with 100 µL of the sample air-dried on glass slides, sputter-coated with gold using Emitech K450X (UK), and analysing the particle size distribution with ImageJ software (Version 1.45, NIH, Bethesda, MD, USA). The Hitachi HF5000 TEM (Hitachi, Tokyo, Japan) was used to obtain high-resolution structural details of the samples prepared on gold grids under vacuum conditions. Surface topography at nanoscale resolution was assessed with the Bruker Dimension XR AFM (Bruker, USA) in contact and tapping modes, using a laser diode and photodetector to capture probe deflection as it scanned the sample surface[34]. This comprehensive set of analyses furnished detailed data on MTX-Lf-SLNs, in support of their stability and structural integrity for pharmaceutical application.

Determination of the encapsulation efficiency (EE%), drug loading (DL), and drug content (DC%)

Samples were centrifuged at 14,000×g for 1 h at 10 °C to determine the encapsulation efficiency (EE%), drug loading (DL), and drug content (DC%) of Methotrexate-loaded solid lipid nanoparticles (MTX-SLNs) and Lactoferrin-conjugated Methotrexate-loaded solid lipid nanoparticles (MTX-Lf-SLNs)[35]. Samples were then quantified of the drug contents in supernatants with a UV-visible spectrophotometer with calibration curves. The EE% was obtained by finding the percentage of total drug that was entrapped within the nanoparticles. The DL was determined to be the mass of the total drug per mass of the nanoparticles. The drug content, DC%, was found to represent the percent drug within the mass of nanoparticles based on the following equation:

$$\text{Entrapment efficacy (EE \%)} = \frac{Total\ drug\ incorporated - Total\ unloaded\ drug}{Total\ drug\ incorporated} \times 100$$

$$\text{Drug Loading (DL) (mg/g)} = \frac{Total\ drug\ incorporated}{SLNs\ Mass}$$

$$\text{Drug content (DC\%)} = \frac{Total\ drug\ incorporated - Total\ unloaded\ drug}{SLNs\ Mass} \times 100$$

Morphological analysis

Samples of MTX-loaded solid lipid nanoparticles (MTX-SLNs) and lactoferrin-conjugated MTX-loaded SLNs (MTX-Lf-SLNs) were washed with PBS before fixation in 2.5% glutaraldehyde solution for 4 h at 4°C[36]. Samples fixed with glutaraldehyde solution were then sequentially treated with ethanol solutions with increasing concentrations: 50, 60, 70, 80, 90, and 100% v/v for 30 min at 4 °C. Samples were air-dried, mounted on aluminum stubs, and coated with a thin layer of gold for scanning electron microscopy (SEM)[37]. The surface morphology was examined by SEM imaging using a ZEISS EVO 18 SEM (Carl Zeiss, Oberkochen, Germany) at an acceleration voltage of 10 kV. Transmission electron microscopy (TEM)[38] was performed using a JEOL JEM-2100 (JEOL Ltd., Tokyo, Japan) operating at 200 kV. Each sample drop was deposited on copper grids, stained with 2% phosphotungstic acid for 1 min, air-dried, and imaged. Atomic force microscopy was conducted by depositing samples onto freshly cleaved mica sheets and scanning them on a Bruker Dimension Icon AFM (Bruker, Billerica, MA, USA) in tapping mode using a silicon nitride cantilever (spring constant: 20–80 N/m). This multi-instrumental approach gave thorough data regarding the size, shape, and surface characteristics of MTX-SLNs and MTX-Lf-SLNs.

Cumulative drug release and drug release kinetic assessment

The cumulative drug release and release kinetics of Methotrexate (MTX)[39] MTX-loaded solid lipid nanoparticles (MTX-SLNs), and Lactoferrin-conjugated MTX-loaded solid lipid nanoparticles (MTX-Lf-SLNs) were evaluated at two pH conditions, i.e., pH 7.4 and pH 5.7, using the dialysis bag method. Dialysis bags of molecular weight cut-off 12–14 kDa (Sigma-Aldrich, Bengaluru, India) were filled with 1 mL of formulations containing either pure MTX at 1 mg concentration or equivalent concentrations of MTX (1 mg MTX per 10 mg nanoparticles) in suspensions of nanoparticles. The bags were submerged in 50 mL of PBS (pH 7.4) or phosphate buffer (PB, pH 5.7) containing Tween 80 (0.1% v/v) to maintain sink conditions, stirred at 100 rpm, and incubated at 37 °C. At predetermined time intervals (1, 2, 4, 6, 8, 12, and 24 h), 1–2 mL of the buffer was withdrawn for analysis and replaced with fresh buffer. MTX concentrations in the samples collected were determined by using a UV-visible spectrophotometer at 302 nm. Cumulative release (%) was calculated, and data were analysed by kinetic models such as Zero-order, First-order, Higuchi, Hixon-Crowell, and Korsmeyer-Peppas to determine the mechanism of release and the best-fit model for each formulation.

The cumulative release (%) was calculated as per given formula: $\frac{Amount\ of\ MTX\ relesed}{Total\ MTX\ loaded} \times 100$

Stability assessment of MTX-SLNs and MTX-Lf-SLNs

The stability of MTX-SLNs and MTX-Lf-SLNs after 3 months storage at 4 °C was checked. Stability was calculated through changes in particle size, zeta potential, leakage of drug, and crystal pattern, which are all compared with the freshly prepared sample. Samples stored and fresh were coated on a glass slide (1 cm^2), air-dried, and analysed using a Tongda TD-3700 XRD instrument (Dandong, Liaoning, China) at a scan range of $2\theta = 10°–60°$ to assess the crystal pattern[40]. The following were the settings of the instrument: 0.02° per 0.5 s was the scan rate, and step size was 0.02°, time per step was 0.5 s, copper anode (target material), Kα wavelength of 1.5406 Å, 30 kV as voltage, and current was 20 mA.

Cell culture procedure for HCT 116 cells with methotrexate and nanoparticle treatments

HCT 116 colon cancer cells were seeded at a density of 1×10^6 cells in T25 flasks containing 3 mL of RPMI-1640 medium supplemented with 10% FBS and 1% penicillin-streptomycin[41]. The incubation was done at 37 °C with 5% CO_2. Three experimental groups for treatment were prepared: (1) Methotrexate (MTX) at a concentration of 10 µM in RPMI medium, (2) MTX-loaded solid lipid nanoparticles (MTX-SLNs) equivalent to 10 µM MTX concentration, and (3) Lactoferrin-conjugated MTX-loaded SLNs (MTX-Lf-SLNs) also at the MTX-equivalent concentration of 10 µM. For each treatment, cells were used for 24 h. After the incubation period, cell viability was determined by an MTT assay.

MTT cytotoxicity/biocompatibility assay

To assess the cytotoxicity of Methotrexate (MTX)[42] MTX-loaded solid lipid nanoparticles (MTX-SLNs), and Lactoferrin-conjugated MTX-loaded SLNs (MTX-Lf-SLNs) in HCT 116 cells, an 3-(4,5-Dimethylthiazol-2-yl)−2,5-diphenyltetrazolium bromide (MTT) assay was carried out using standard procedures. HCT 116 cells[43] were obtained from the National Centre for Cell Science, Pune, India. Cells were maintained in Dulbecco's Modified Eagle Medium (DMEM) containing 10% fatal bovine serum and 1% antibiotic solution. Cells were maintained at 37 °C in a humidified incubator supplemented with 5% CO_2 and plated at 10,000 cells/well in 96-well plates to adhere for 24 h. The cells were subsequently exposed to a range of concentrations of MTX as well as MTX-SLNs and MTX-Lf-SLNs along with free MTX dissolved in DMSO for control. After 24-hour incubation with the test compounds, 20 µL of MTT solution was added to each well, and plates were further incubated at 37 °C for an additional 2 h for the reduction of MTT to formazan by metabolically active cells. The medium was removed with care and 100 µL of DMSO was added to dissolve purple formazan crystals developed[44]. The absorbance was read at a wavelength of 540 nm having a reference wavelength of 660 nm in an ELISA plate reader (iMark, Biorad, USA). Viabilities of the cells were determined relative to control cells, which were left untreated, and IC50 values, the concentration of each compound necessary for a 50% growth inhibition in

cell growth, were obtained by GraphPad Prism 7 software. The present assay permitted the cytotoxic potency comparison of MTX, MTX-SLNs, and MTX-Lf-SLNs on HCT 116 cells.

Cellular apoptosis

The study assessed cellular apoptosis of Methotrexate (MTX) induced by MTX-loaded solid lipid nanoparticles (MTX-SLNs), Lactoferrin-conjugated MTX-loaded SLNs (MTX-Lf-SLNs) in HCT 116 cells by flow cytometry[45]. The cells were incubated with 1.8 µg/mL of MTX, 0.9 µg/mL of MTX-SLNs, and 0.4 µg/mL of MTX-Lf-SLNs. The control for vehicle was set equivalent to the concentration of solvent used for MTX-Lf-SLNs. Cells were then aliquoted into five groups: unstained cells, control, Prolium Iodide (PI), Annexin V, and treatment groups. All cells were resuspended in 1X binding buffer at 1×10^6 cells/mL. To the labelled tubes of the treatment groups, Annexin V-FITC was added to bind phosphatidylserine exposed on apoptotic cells and PI, which marks necrotic or late-apoptotic cells with compromised membranes. Samples were vortexed gently and incubated at room temperature in the dark for 15 min. Post incubation, the cells were resuspended into 400 µL of binding buffer at 1X concentrations and were immediately analysed via BD FACS-Canto II flow cytometer[46]. Flow cytometry was used to differentiate live, early apoptotic, late apoptotic, and necrotic cells based on Annexin V-FITC and PI staining patterns, which allows the quantification of apoptotic cells induced by MTX, MTX-SLNs, and MTX-Lf-SLNs in comparison with controls.

DAPI staining

Nuclear morphological changes in HCT 116 cells treated with Methotrexate (MTX)[47] MTX-loaded solid lipid nanoparticles (MTX-SLNs), and Lactoferrin-conjugated MTX-loaded SLNs (MTX-Lf-SLNs) were evaluated through 4',6-Diamidino-2-phenylindole (DAPI) staining. As per the procedure, glass coverslips were placed in 6-well plates, and 4×10^5 cells were seeded per well. Following 48 h of treatment of the different samples, plain drugs as well as MTX-loaded nanoparticles, the media was removed and cells were fixed in 4% paraformaldehyde for 45 min at room temperature (24 ± 2 °C). Then the cells were permeabilized for 3 min with 0.5% Triton X-100, and stained for 20 min with 20 ng/mL DAPI[48]. Then coverslips were washed using PBS, placed over slides and morphological changes at nuclear levels were observed through an Olympus IX81 motorized fluorescence microscope fitted with an Olympus DP72 digital camera. To have quantitative analysis of these observations, nuclear area measurement was done using the software of ImageJ according to the method given by Jon R. Eidet. Micrographs were converted to 8-bit images, threshold adjustments were made, non-nuclear fragments were removed, and nuclei were segmented using the "Watershed" function. The "Analyze Particles" tool was used to quantify nuclear areas for 100 cells per treatment, and the data were normalized to the control group.

Acridine orange/propidium iodide (AO/PI) dye exclusion assay into the cellular uptake procedure for HCT 116 cells

HCT 116 cells were plated in six-well culture plates at a density of 4×10^5 cells/well and incubated at 37 °C with 5% CO_2 for 24 h. Following incubation, the cells were exposed to Methotrexate (MTX), MTX-loaded solid lipid nanoparticles (MTX-SLNs), or Lactoferrin-conjugated MTX-loaded SLNs (MTX-Lf-SLNs) at a concentration of 20 µg/mL for 30 min and 1 hour[49]. After incubation, the cells were washed three times with PBS, trypsinized, spun at 300 × g for 6 min, and then their respective pellets re-suspended in PBS. After that, to this cell suspension, 1: 1 of mixture of both dyes- AO (10 µg/mL) as well as PI (10 µg/mL) in concentration- were added with incubation time in a dark chamber for 10 min at room temperature[50]. Stained cells were observed using a fluorescence microscope to observe the morphological changes where the viable cells were green in color, and the apoptotic cells appeared orange to red due to the condensation of nuclei and membrane blebbing. Fluorescence microscopy was used for quantitative analysis of viable and apoptotic cells. Viable cell numbers were reduced and there was an increase in the apoptotic cells, significantly enhanced with Lactoferrin-targeted Nano formulation MTX-Lf-SLNs confirming that it has an apoptotic potential in HCT 116 cells.

ROS estimation protocol for MTX and its formulations

To evaluate ROS generation of HCT116 cells subjected to Methotrexate (MTX), MTX-loaded solid lipid nanoparticles (MTX-SLNs), and Lactoferrin-conjugated MTX-loaded SLNs (MTX-Lf-SLNs), HCT116 cells were seeded in 6-well plates at a cell density of 50,000-100,000 cells in DMEM with 10% FBS and 1% antibiotic concentration and incubated for 24 h at 37 °C having 5% CO_2 concentration[51]. After this, cells were exposed to the fresh medium that contained each test compound and incubated for an additional 24 h. The medium was removed, and cells were collected with trypsin-EDTA. They were then washed twice with cold PBS and resuspended in PBS containing 2 µM 2',7'-Dichlorodihydrofluorescein diacetate (DCFDA) for ROS detection[52]. The cell suspensions were incubated in the dark for 30 min, and fluorescence intensity, which reflects ROS levels, was measured within an hour using a BD FACS Calibur flow cytometer. Data analysis with FCS Express 7 (Version 7, De Novo Software, Glendale, California, USA) quantified ROS levels, allowing comparison across treatments to evaluate oxidative stress potential induced by MTX, MTX-SLNs, and MTX-Lf-SLNs.

Mitochondrial membrane potential (MMP) assay

To evaluate MMP in Methotrexate (MTX)-treated HCT-116 cells, MTX-loaded solid lipid nanoparticles (MTX-SLNs), and Lactoferrin-conjugated MTX-loaded SLNs (MTX-Lf-SLNs), HCT-116 cells were grown in appropriate growth media and incubated at 37 °C with 5% CO_2[53]. Later, the cells were treated for 24 h with IC50 concentrations of each formulation, along with a positive control, e.g., CCCP for confirming mitochondrial depolarization. Following treatment, cells were dispersed, pelleted, and washed with cold PBS to remove residual trypsin-EDTA. The cell pellet was then stained with 2 µM JC-1 dye, a fluorescent dye that accumulates in healthy mitochondria, emitting red fluorescence in polarized (healthy) mitochondria and green fluorescence in

depolarized (unhealthy) mitochondria. Following incubation in the dark for 15–30 min, cells were analyzed by flow cytometry to detect red and green fluorescence intensities with at least 10,000 events recorded per sample. A higher red-to-green fluorescence ratio indicated healthier mitochondrial function, while a lower ratio suggested mitochondrial depolarization, providing a quantitative comparison of MMP across MTX, MTX-SLNs, and MTX-Lf-SLNs treatments in HCT-116 cells.

Biomarker expression analysis of caspase-6 in HCT116 cells by immunofluorescence
To evaluate Caspase-6 expression in HCT 116 cells via immunofluorescence, seed 1×105 cells per well in 6-well plates with 2 mL complete growth medium. Incubate overnight at 37 °C in a humidified 5% CO_2 environment. Add the following to the cells: control group with 2 mL complete growth medium; 10 µM Methotrexate (MTX) for the MTX group; MTX-loaded solid lipid nanoparticles (MTX-SLNs) equivalent to 10 µM MTX; and Lactoferrin-conjugated MTX-loaded SLNs (MTX-Lf-SLNs) also equivalent to 10 µM MTX. Following 24-hour treatment at 37 °C, remove the medium and wash cells three times with 2 mL PBS for 5 min each. Fix with 2 mL of 4% paraformaldehyde for 15 min at room temperature, then rinse three times with PBS. Permeabilize with 2 mL of 0.1% Triton X-100 in PBS for 10 min and wash three times with PBS. Block non-specific binding with 2 mL of 5% BSA in PBS for 1 h. Add the Caspase-3 primary antibody diluted 1:200 in blocking solution overnight at 4°C[54]. Wash the cells the next day three times in PBS and add a 1:500 dilution of Alexa Fluor 488-conjugated secondary antibody in blocking solution and leave for 1 h at room temperature in the dark. Use three further PBS washes to complete the staining by adding a 1 µg/mL DAPI solution for 5 min. Place the cells onto glass slides and capture pictures with a fluorescence microscope through filters for Alexa Fluor 488 green and DAPI blue. An analyze Caspase-6 expression by fluorescence intensity across the groups.

Migration assay
For determining the invasion of Methotrexate (MTX)-treated HCT 116 cells, MTX-loaded solid lipid nanoparticles (MTX-SLNs), and Lactoferrin-conjugated MTX-loaded SLNs (MTX-Lf-SLNs), the assay involved conducting a migration assay. The cells were seeded at a density of 2×10^5 cells per well in a 24-well culture plate. After 24 h, the medium was removed and a scratch was created on each cell monolayer using a 200 µL pipette tip. The wells were then washed three times with PBS to remove debris[55]. The cells were treated with different test compounds: MTX, MTX-SLNs, and MTX-Lf-SLNs; where untreated cells served as the control. Migration and scratch closure were monitored and quantified using an Olympus CKX41 inverted microscope, and the images were analysed with CellSens software (version 3.3). The scratch closure extent for each treatment group was compared with the negative control to determine the effect on cell migration.

Immunogenicity valuation in HCT116 cells
HCT116 colon cancer cells are cultured in DMEM medium containing 10% FBS and 1% penicillin-streptomycin at 37 °C under 5% CO_2 incubation and seeded at a density of 5×10^5 cells/well in 6-well plates, to support adhesion overnight. Cells are incubated for 48 h with different formulations, including untreated control, free Methotrexate (MTX) 10 µg/mL, MTX-Solid Lipid Nanoparticles (MTX-SLNs) at an equivalent dose of MTX, MTX-Lactoferrin-Conjugated SLNs (MTX-LF-SLNs) at the equivalent dose of MTX, and Lipopolysaccharide (LPS) 1 µg/mL positive inflammation control. Following incubation, cytokine release (IL-6, TNF-α, IL-1β) is quantified by an enzyme-linked immunosorbent assay (ELISA) on the Epoch 2 Microplate Spectrophotometer (Epoch2BioTekInstruments, Inc.,Winooski, Vermont, USA), from the culture supernatants harvested, Immune activation markers, including Intercellular Adhesion Molecule-1 (ICAM-1, CD54) and Human Leukocyte Antigen-DR (HLA-DR, MHC class II), are established by flow cytometry on the BD FACSCanto II Flow Cytometer (FACSCanto II, BD Biosciences, San Jose, California, USA).

Cytokine release assay (ELISA Analysis) After incubation for 48 h, treated and control HCT116 cell culture supernatants are slowly transferred to sterile microcentrifuge tubes and centrifuged at 1,500 rpm for 10 min at 4 °C to discard the cellular debris. Clear supernatants are poured into new tubes and stored at −80 °C until analysis. The levels of pro-inflammatory cytokines, such as Tumor Necrosis Factor-alpha (TNF-α), Interleukin-6 (IL-6), and Interleukin-1 beta (IL-1β), are measured by commercially available enzyme-linked immunosorbent assay (ELISA) kits (Bhat Biotech India Pvt Ltd) according to the manufacturer's guidelines. Following three washes with the given wash buffer, 100 µL biotin-conjugated detection antibodies anti-TNF-α (Catalog No: BBITN-Fα-ELISA, 1:1000 dilution), anti-IL-6 (Catalog No: BBIIL6-ELISA, 1:800 dilution), and anti-IL-1β (Catalog No: BBIIL1β-ELISA, 1:1200 dilution) are placed in the corresponding wells and incubated at 37 °C for 1 h. Following a second wash step, 100 µL horseradish peroxidase (HRP)-streptavidin solution is added and incubated for 30 min in the dark. After a final wash step, 90 µL of TMB (3,3′,5,5′-tetramethylbenzidine) substrate solution is added to each well and incubated at room temperature for 15–20 min, permitting the development of colour. The reaction is terminated by adding 50 µL of stop solution and the absorbance is read immediately at 450 nm using a microplate reader. Cytokine levels are calculated by referencing absorbance values to a standard calibration curve prepared from known cytokine levels, and results are reported in pg/Ml.

Immune activation marker expression (flow cytometry) The cells are collected post-treatment, rinsed two times with PBS (pH 7.4, 1 mL per well), and lysed by the action of 0.25% Trypsin-EDTA (200 µL per well) for 3 min at 37 °C. Neutralization is performed using 1 mL complete DMEM medium and centrifugal recovery at 1500 rpm for 5 min at 4 °C. The pellet is twice washed with cold PBS 1 mL, blocked with 200 µL of 2% BSA PBS for 15 min at room temperature, and stained with Anti-ICAM-1-PE (1:200, eBioscience, Catalog No: 12-0549-42) and Anti-HLA-DR-FITC (1:250, eBioscience, Catalog No: 11-9956-42) in 100 µL PBS per sample on ice for 30 min in the dark. After washing with two PBS washes, cells are re-suspended to a concentration of 500 µL

FACS buffer (2% FBS, 0.1% sodium azide in PBS) and are processed for analysis through a BD FACSCanto II Flow Cytometer (FACSCanto II, BD Biosciences, San Jose, California, USA), recording 10,000 events/sampling. Analysis of data is carried out with Flowing Software (Turku Bioscience, Finland) following appropriate gating strategies and fluorescence compensation to obtain mean fluorescence intensity (MFI) and percentage expression of ICAM-1 and HLA-DR. The experiment is carried out in triplicate, and statistical analysis is carried out using GraphPad Prism software.

CAM assay for angiogenesis investigation

MTX, MTX-loaded solid lipid nanoparticles (MTX-SLNs) and lactoferrin-conjugated MTX-loaded SLNs (MTX-Lf-SLNs) were studied for their potential in the angiogenesis investigation by the CAM assay, to observe the effects of these drugs on the CAM of fertilized Gallus gallus domesticus chicken eggs[56]. Fertilized eggs were initially incubated at 37.5 °C with 60% humidity till day 11 of embryonic development. On day 11, a small window was carefully created over a prominent blood vessel site on each egg. Sterile discs carrying the treatment samples (MTX-SLNs and MTX-Lf-SLNs) were placed on the exposed CAM area. For comparison, discs carrying PBS served as the negative control while Avastin (25 mg/mL) served as the positive control for angiogenesis inhibition. The eggs were observed for 48 h, following which images were captured for analysis. The images were processed using ImageJ software, converting the images into 8-bit format, adjusting the threshold for enhancement of blood vessels, and calculating the area covered by blood vessels and normalizing them against the negative control for evaluation of angiogenesis suppression brought about by the treatments.

Results

Methotrexate binding affinities and interactions

Methotrexate has shown different affinities towards the target proteins; however, the highest interaction was seen with Caspase-6 (PDB ID: 3OD5), which has a docking score of −9.316 and Glide energy of −43.99. Such high affinity is caused due to the presence of both hydrophobic, polar, and electrostatic interactions. The hydrophobic contact formed with residues such as Phe263, Cys264, and Val261 results in a non-polar environment that enhances the binding stability of Methotrexate. Polar interactions with Ser218 and Tyr217 further stabilize the ligand through a network of supportive hydrogen bonds. Electrostatic interactions with Arg220, Glu221, and Asp262 set up an even more substantial charged network, thus favouring the orientation of the ligand and its retention within the pocket (Fig. 2a). In addition, Methotrexate forms crucial hydrogen bonds with Arg220, Glu221, and Asp262, which largely contribute to the stability and specificity of the binding. Methotrexate's planar configuration and conjugated ring structure allow for an excellent fit in the binding pocket, thus optimizing its interactions with adjacent residues. For AKT protein (PDB ID: 3AOX), Methotrexate displayed a moderate stability with a docking score of −5.817 and Glide energy of −37.03. It showed interaction with several BCL2 proteins, with docking scores of −5.281, −5.345, −4.854, and − 4.408, and corresponding Glide energies of −45.563, −42.82, −39.65, and − 35.15 for PDB IDs 1GJH, 4LXD, 4IEH, and 6O0K, respectively. The interaction with BCL2 (PDB ID: 1GJH) was the strongest, implying moderate binding stability. The docking interaction of Methotrexate with Bcl-xL protein (PDB ID: 2YXJ) was weaker: the docking score was about − 4.415 whereas the Glide energy was about − 35.33. Methotrexate showed moderate levels of interaction with Caspase-3 (PDB ID: 1PAU) with a docking score at −4.637 along with a Glide energy of around − 37.16 whereas its interaction with Caspase-9 (PDB ID: 1JXQ) was relatively less, with a docking score of −3.384 and Glide energy of approximately − 43.12. Ligand's binding to CD44 resulted in a docking score of −3.51 and Glide energy of −33.38, meaning lower binding affinity. In EGFR proteins, Methotrexate showed a diverging range of binding, reaching a docking score of −4.948 and Glide energy of −49.04 with EGFR (PDB ID: 1M17). On the other hand, its interaction with EGFR (PDB IDs: 1XKK and 3POZ) was relatively weaker. Its docking scores were − 3.946 and − 2.325, and Glide energies were − 55.44 and − 42.9, respectively. Methotrexate's interaction with the MMP7 protein (PDB ID: 2Y6C) resulted in stable binding with a docking score of −5.144 and Glide energy of −48. 631. Methotrexate demonstrated the highest binding affinity and stability with Caspase-6, suggesting the selectivity and efficacy potential against this target, supported by the interplay of hydrophobic, polar, and electrostatic interactions, and critical hydrogen bonds within the binding pocket (Fig. 2b).

Wen Li et al.[57] showed that methotrexate binds with bovine serum albumin (BSA) mainly through static quenching mechanisms at Site I, with binding constants of 2.30 × 105 M at 301 K. Thermodynamic parameters indicated that van der Waals forces and hydrogen bonds were the driving forces for the complexation, as evidenced by the negative Gibbs free energy of the process, Δ∘= −30.96 kJ/mol. Molecular docking showed binding energy of − 6.22 kcal/mol, which means there is a stable complex. Methotrexate interactions slightly changed the secondary structure of BSA, which involved a minor decrease in the contents of α-helix from circular dichroism spectroscopy. Our work draws parallel with Wen Li et al. by studying molecular docking properties of methotrexate, identification of binding sites, stability factors and interaction forces such as hydrophobicity and hydrogen bonding. Both studies exhibit excellent binding affinities but through different proteins and emphasize methotrexate's structural flexibility as well as interaction-induced conformational changes.

Molecular dynamics results of methotrexate-caspase-6 complex

Docking study have shown binding of methotrexate to the Caspase-6, BCL-2 and MPP-7. We performed MD studies understand the dynamic behaviour of methotrexate in these complexes. The equilibration was performed for 10 ns while production was continued subsequently for 40 ns. RMSD analysis of proteins during the simulation showed that protein-methotrexate complexes are stable (Fig. 2c) RMSD analysis of methotrexate was also performed to understand the stability within the active site of these proteins. It is shown in the Fig. 2d. During the simulation methotrexate found to have formed interactions with the Caspase-6 residues viz. Arg64, Gln161, Asn166, Hie168, Tyr217, Arg220, Thr222, Lys265, Asp266, and Ser268. Interactions with these residues

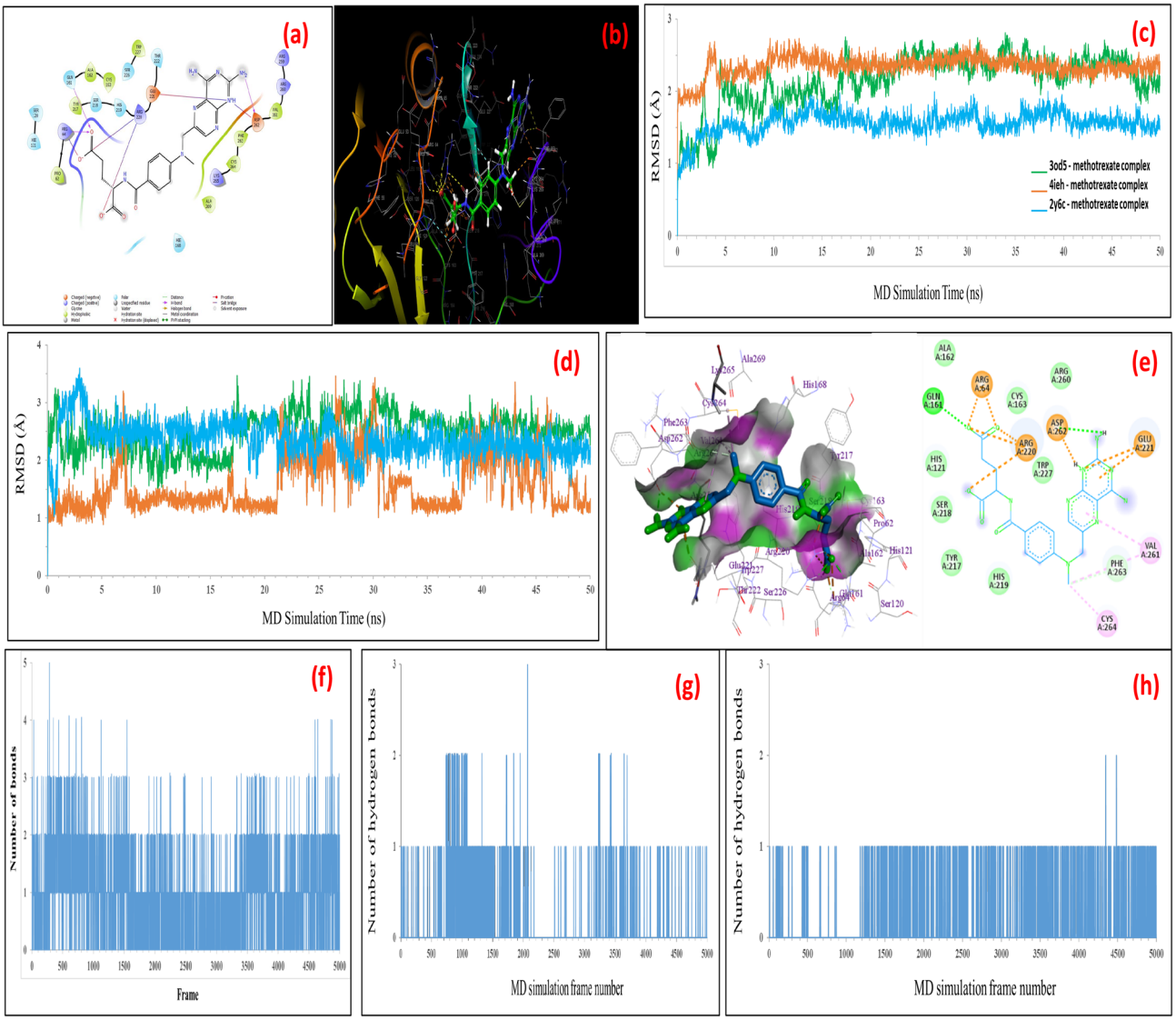

Fig. 2. **(a)** 2D Interaction Map: Shows binding interactions between MTX and Caspase-6 residues, including hydrophobic contacts with Phe263, Cys264, and Val261; hydrogen bonds with Ser218 and Tyr217; and electrostatic interactions with Arg220, Glu221, and Asp262. These interactions increase binding stability and specificity. **(b)** 3D Binding Pocket Visualization: Illustrates the placement of MTX within the Caspase-6 binding site, showing how hydrophobic, polar, and electrostatic interactions cooperate to optimize ligand positioning and binding. **(c)** Root means square deviation of backbone atoms of Caspase-6, BCL-2 and MPP-7 in complex with methotrexate during 50 ns MD simulation. **(d)** Root mean square deviation of methotrexate in the complex of Caspase-6 (green colour), BCL-2 (orange colour) and MPP-7 (blue colour) complex in the 50 ns MD simulation. **(e)** 3D interaction map of methotrexate with Caspase-6 B- 2D interaction map of methotrexate. **(f)** Hydrogen bong interactions between methotrexate and Caspase-6 residues throughout the 50 ns MD simulation. **(g)** Hydrogen bong interactions between methotrexate and BCL-2 residues throughout the 50 ns MD simulation. **(h)** Hydrogen bong interactions between methotrexate and MPP-7 residues throughout the 50 ns MD simulation.

are depicted in Fig. 2e. It reveals that carboxyl groups of methotrexates were involved in formation of ionic interactions with basis residues such as Arg64 and Arg220. Pi stacking interactions were formed by Trp227, Phe263 and Tyr217. In addition to these interactions methotrexate formed at least 2 hydrogen bond interactions with surrounding residues throughout the 50 ns simulation (Fig. 2f). However, methotrexate showed weaker binding with BCL-2 and MPP-7. As can be seen from Fig. 2g and h. It formed inconsistent hydrogen bond interactions with them. This result was in line with the docking score where methotrexate showed highest binding affinity to the Caspase-6 while weaker binding affinity to the BCL-2 and MPP-7.

Fan Xu et al.[58] found that the methotrexate-cisplatin complex (cis-[Pt(NH3)2MTX]) exhibited increased molecular stability via intra- and intermolecular hydrogen bonds, with interaction energies of − 811.76 kcal/mol − 811.76 kcal/mol for the complex compared to − 780.87 kcal/mol − 780.87 kcal/mol for cisplatin. The molecular

docking showed a binding energy of − 11.9 kcal/mol − 11.9 kcal/mol to folate receptors; the key residues were identified as ASP81 and SER174, which contributed by hydrogen bonds with bond lengths of 2.803 Å and 2.843 Å, respectively. Molecular dynamics simulations further confirmed that the complex was thermodynamically stable with improved cancer-targeting capabilities. Our study showed that Methotrexate was stably bound to Caspase-6 throughout the molecular dynamics simulations with very low RMSD fluctuations and persistent interactions. Similarly, Fan Xu et al. showed improved thermodynamic stability of the methotrexate-cisplatin complex through hydrogen bonding. Both studies highlighted the role of Methotrexate in forming stable complexes and its potential as a therapeutic agent.

Scalability and reproducibility of lactoferrin conjugation

The refined conjugation technique achieved a consistent Lf attachment efficiency of 83 ± 2.5%, showing low variability between batches. Surface adsorption resulted in a marginally reduced efficiency (73 ± 4.13%) but showed improved scalability. The microfluidic-assisted method enhanced consistency and cut reaction time by 40% in comparison to traditional stirring-based conjugation. These results indicate that surface adsorption and microfluidics provide practical options for enhancing scalability without notably reducing efficiency. Upcoming research will aim at further refining reaction parameters and investigating click chemistry-based conjugation for improved reproducibility (Table 1). Future research may investigate click chemistry-based conjugation or enzyme-driven methods, which could further streamline the process and enhance reproducibility in industrial uses.

Linearity and precision of methotrexate quantification by UV-visible spectroscopy and HPLC

The methotrexate standard curves prepared both by using UV-Visible spectroscopy and HPLC gave excellent linearity in concentration range 2–10 µg/mL. In the case of UV-Visible spectroscopy, absorbance measured at 302 nm gave excellent linear correlation with concentration which resulted in an R^2 value of 0.9985 (Fig. 3a). Similarly, the HPLC method using a C18 column and a phosphate buffer-acetonitrile mobile phase (70:30 v/v) had a strong positive linear relationship between peak area and concentration, with an R^2 value of 0.9992. For MTX, the HPLC retention time, which was determined to be 0.96 ± 0.02 min, showed good method reproducibility (Fig. 3b). While both methods were reliable, HPLC was much more sensitive, as it gave a steeper slope in the standard curve. Hence, this method is more suited to detection of lower concentrations of MTX. These results have confirmed the precision and reproducibility of UV-Visible spectroscopy and HPLC for MTX quantification, but the latter is slightly more sensitive.

Interpretation on FTIR and DSC spectra

The FTIR spectra of all samples indicated a fingerprint area with characteristic peaks from 1800 to 600 cm^{-1}, indicating several functional groups and confirming the complexity in the spectra due to a few compounds with different functionalities. For MTX, C = O stretching for amide group is at 1741.58 cm^{-1}. In case of C-H stretching of aliphatic CH2 and CH3 groups, it has values of 2856.41 and 2907.24 cm^{-1}, respectively. There is a peak at 1697.88 cm^{-1} from a carboxylic acid group, possibly from a lipid component, and another one at 2380.15 cm^{-1} from a combination band or overtone in the physical mixture spectrum, which mimics the MTX spectrum. MTX-SLNs spectrum shows peaks of MTX and lipid components such as amide-associated peak at 1741.58 cm^{-1} and C-H stretching vibrations of aliphatic CH2 and CH3 groups from the lipid matrix at 2929.54 and 3288.96 cm^{-1}. The MTX-Lf-SLNs spectrum is more complex with a shifted peak at 1756.74 cm^{-1} that may be attributed to lactoferrin interactions, and peaks at 2929.54 and 3288.96 cm^{-1} that indicate lipid components. A high peak at 3398.66 cm^{-1} shows O-H stretching vibrations of hydroxyl groups in lactoferrin. The FTIR spectra of the conjugated samples clearly support the encapsulation efficiency of MTX into lipid nanoparticles and conjugation of lactoferrin with alterations in the positions of peaks and new peaks arising in the MTX-Lf-SLNs spectrum, indicating the interactions of drug, lipid, and protein. FTIR spectra are complex, and thus peak assignment requires more information and comparison of the spectra with reference spectra (Fig. 3c). DSC profiles, which plot heat flow versus temperature, indicate material thermal transitions. In phase transitions, such as melting, peaks are endothermic while absorbing energy, and peaks are exothermic while releasing energy. MTX's DSC curve consists of one endotherm at 177.65 °C, its melting point. The placebo curve is complex in pattern with several endothermic peaks, one of which is at roughly 159.42 °C that may be associated with the melting of a lipid component, while another is at 218.70 °C, perhaps associated with a different lipid or an excipient. In the case of MTX-SLNs, a larger endothermic peak was recorded around about 165.79 °C which slightly shifts as compared to pure MTX (Fig. 3d). This shows the encapsulation of MTX into lipid nanoparticles and it indicates that the melting is a result of the lipid matrix. In MTX-Lf-SLNs, a large endothermic peak was recorded at 299.17 °C that infers stabilization of MTX in the nanoparticle upon conjugation with lactoferrin. The DSC profile collectively verifies the effective encapsulation of MTX within lipid nanoparticles and its stabilization

Parameter	Carbodiimide Bonding	Surface Adsorption
Conjugation Efficiency (%)	83 ± 2.5	73 ± 4.13
Response Duration (h)	4	6
Variability from Batch to Batch	Low	Moderate
Scalability Capability	Moderate	High

Table 1. Scalability and reproducibility of lactoferrin Conjugation.

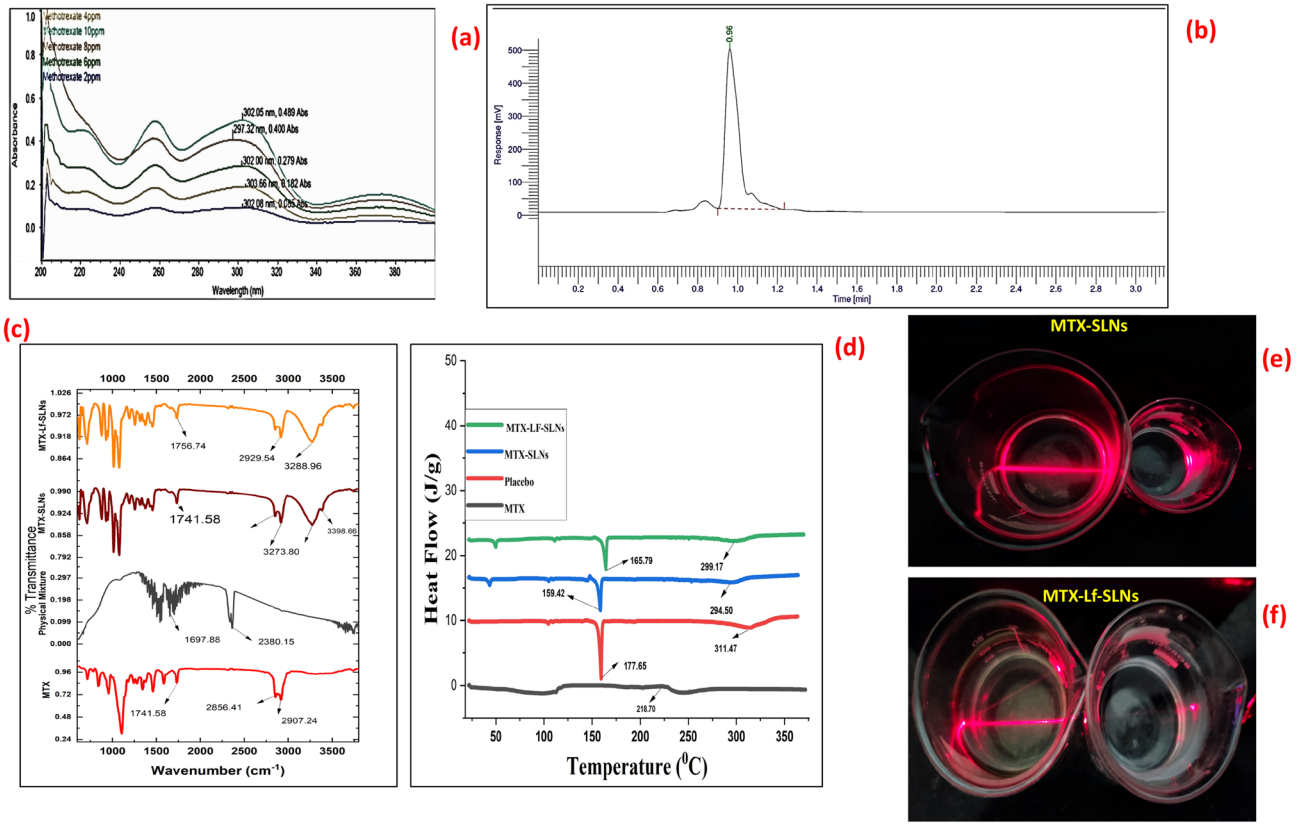

Fig. 3. **(a)** Overlay plot of UV-Visible spectroscopy for Methotrexate (MTX) at 302 nm, revealing distinct absorption peaks across different concentrations ranging from 2–10 µg/mL. **(b)** RP-HPLC chromatogram for Methotrexate (MTX) exhibits a retention time of 0.96 min, confirming the purity and identification of MTX within the formulations prepared. **(c)** FTIR spectra for MTX, placebo SLNs, MTX-SLNs, and MTX-Lf-SLNs present characteristic functional group peaks, validating successful encapsulation and conjugation with lactoferrin. **(d)** DSC thermograms for MTX, placebo SLNs, MTX-SLNs, and MTX-Lf-SLNs display melting points and thermal transitions, suggesting stable nanoparticle formulations and efficient drug incorporation. **(e)** Tyndall effect noted in MTX-SLNs dispersion when exposed to laser light, affirming the colloidal character and stability of the nanoparticle suspension. **(f)** Tyndall effect detected in MTX-Lf-SLNs dispersion, indicating enhanced colloidal stability and homogeneity of lactoferrin-conjugated nanoparticles compared to those without conjugation.

through lactoferrin conjugation, as it can be proved through changes in peak locations and peak broadening that reflects the interactions between drug, lipid, and protein components.

Rahul Shah et al.[59] reported that the methotrexate-loaded polysarcosine microspheres were spherical in shape and had a size range of 10–20 µm. FTIR spectroscopy showed major peaks of methotrexate at 1529.24 cm − 1 and 1616.36 cm − 1 due to aromatic C = C stretches, while a broad peak at 3392.23 cm − 1 was due to O-H and N-H stretches. DSC revealed that methotrexate was transformed into an amorphous state, as no crystalline peak was observed at 145 °C. The enthalpy changes were indicative of molecular dispersion within the polymer matrix. The encapsulation efficiency was found to be 86.37%, while the microspheres exhibited 100% drug release in 8 h, optimized for sustained therapeutic action. Our study showed FTIR peaks indicating methotrexate encapsulation and interaction with the polymer, which was in accordance with Rahul Shah et al., where they have observed characteristic peaks like aromatic C = C at 1529.24 cm^{-1}. In both the studies, DSC analysis indicated transitions to amorphous states with absent crystalline peaks and enthalpy changes, confirming molecular dispersion in the polymer matrix.

Tyndall effect and its correlation with MTX-SLNs and MTX-Lf-SLNs

The Tyndall effect proves the nanoscale nature and colloidal stability of Methotrexate-loaded solid lipid nanoparticles (MTX-SLNs) (Fig. 3e & Fig. 4a) and Lactoferrin-conjugated MTX-Lf-SLNs (Fig. 3f & Fig. 4a). MTX-SLNs exhibited a particle size of 145.67 ± 7.56 nm (Fig. 4b), while the particle size of MTX-Lf-SLNs increased to 154.18 ± 8.26 nm (Fig. 4c) as the addition of a proteinaceous Lactoferrin layer on it augmented its hydrodynamic diameter. The zeta potential shifted from − 23.89 ± 4.11 mV (Fig. 4d) for MTX-SLNs to −33.37 ± 4.11 mV (Fig. 4e) for MTX-Lf-SLNs, attributed to Lactoferrin's carboxyl and amino groups, enhancing the surface charge and colloidal stability. These surface modifications alter the optical and physicochemical properties, improving dispersion uniformity and biological interactions. The Tyndall effect observed and zeta

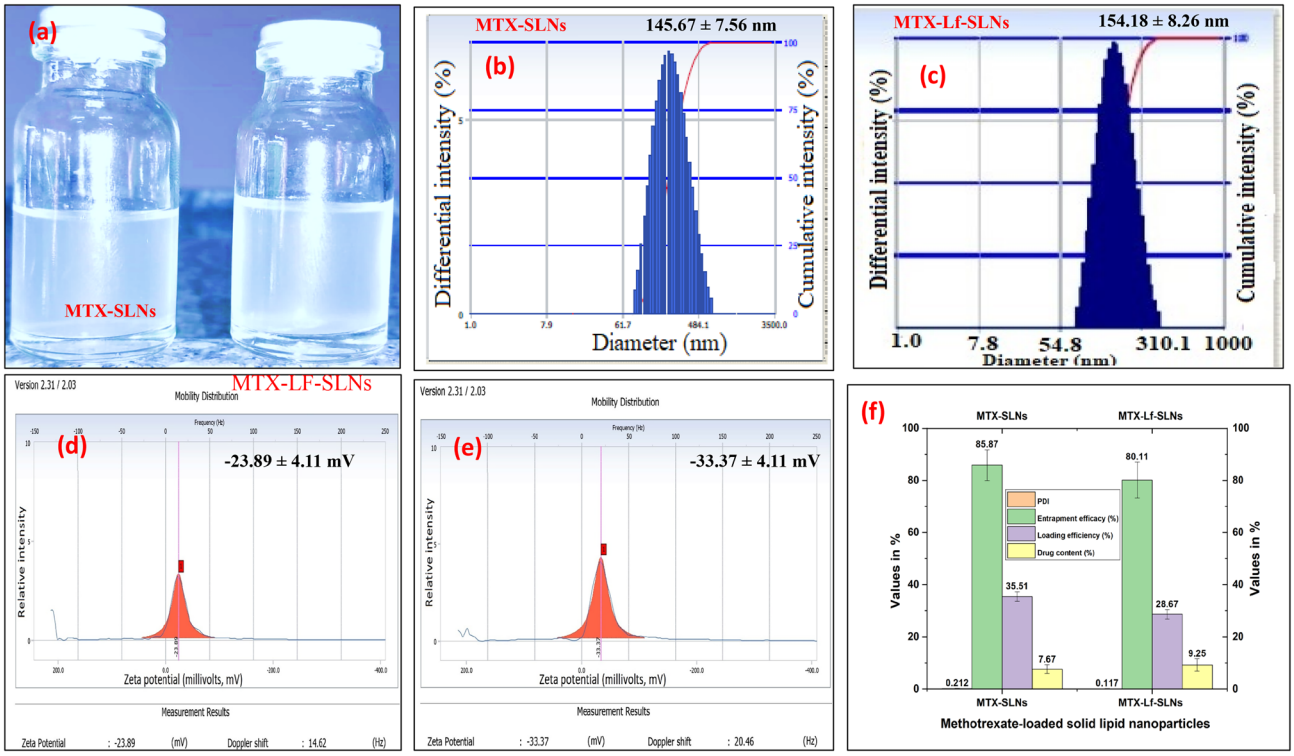

Fig. 4. **(a)** The visual characteristics of Methotrexate-loaded solid lipid nanoparticles (MTX-SLNs) and Lactoferrin-conjugated MTX-Lf-SLNs after they have been dispersed showed a uniform suspension with a noticeable Tyndall effect, indicating well-maintained colloidal properties. **(b)** The particle size distribution for MTX-SLNs indicates an average size of approximately 145.67 ± 7.56 nm, featuring consistent particle sizes and a stable dispersion. **(c)** MTX-Lf-SLNs exhibit an average size of 154.18 ± 8.26 nm, suggesting a minor increase in size due to the addition of the Lactoferrin layer. **(d)** The zeta potential measurement of MTX-SLNs resulted in a value of −23.89 ± 4.11 mV, reflecting moderate stability of the colloids owing to the negative surface charge. **(e)** The zeta potential of MTX-Lf-SLNs was found to be −33.37 ± 4.11 mV, attributed to the Lactoferrin coating, which is thought to enhance electrostatic repulsion and overall stability. **(f)** A comparison of the PDI, entrapment efficiency (EE%), drug content (DC%), and drug loading (DL%) between MTX-SLNs and MTX-Lf-SLNs. The encapsulation efficiency of MTX-Lf-SLNs appears to be slightly reduced at 80.11% compared to MTX-SLNs (85.87%), yet the drug content considerably improved following the Lactoferrin coating application.

Sample	Height (nm)	Roughness (nm)	Kurtosis	Skewness
MTX-SLNs	108 ± 2.5	7.5 ± 0.4	0.70 ± 0.08	−0.39 ± 0.07
MTX-Lf-SLNs	126 ± 2	9.2 ± 0.2	0.80 ± 0.02	−0.50 ± 0.07

Table 2. AFM analysis of MTX-SLNs and MTX-Lf-SLNs showing height, roughness, kurtosis, and skewness.

potential shifts reveal the structural integrity, stability, and functionalization of these nanoparticles, which is essential for effective drug delivery.

Entrapment efficiency, drug content, and loading efficiency of MTX-SLNs and MTX-Lf-SLNs

The encapsulation efficiency (EE%) for Methotrexate-loaded solid lipid nanoparticles (MTX-SLNs) was 85.87%, while for Lactoferrin-conjugated MTX-Lf-SLNs, it is reduced to a little bit, that is, 80.11%. Drug content (DC%) increased from 7.67% in MTX-SLNs to 9.25% in MTX-Lf-SLNs, whereas drug loading (DL%) decreased from 35.51% in MTX-SLNs to 28.67% in MTX-Lf-SLNs (Fig. 4f). Lactoferrin plays a dual role in these formulations. The addition of Lactoferrin, a glycoprotein, introduces carboxyl and amino groups on the nanoparticle surface, allowing it to achieve greater electrostatic interactions with Methotrexate molecules. This accounts for the slight increase in DC%. Lactoferrin can enhance the surface binding capacity and thus contribute to increasing DL%. However, there would be a relative DL% decrease because the incorporation of the Lactoferrin as the coating layer increases the nanoparticle mass. Biophysically, the Lactoferrin coating improves the nanoparticles stability and biocompatibility. It also contributes to a more negative zeta potential and enhances colloidal stability due to increased electrostatic repulsion.

The methotrexate-loaded solid lipid nanoparticles (MTX-SLNs) developed by Md. Abul Barkat et al.[60] resulted in an impressive entrapment efficiency of 87%. This meant that this developed formulation was able to achieve substantial drug encapsulation inside the nanoparticles. The amount of drug loaded into this developed formulation was also extremely high, with a drug-loading capability of 62.92%. These results highlight the promise of MTX-SLNs as an effective drug delivery system that provides improved therapeutic efficacy with enhanced encapsulation, controlled release, and targeted delivery. Our study and Md. Abul Barkat et al. focused on methotrexate-loaded SLNs, which had high encapsulation efficiency (85.87% vs. 87%) and drug content, and our Lactoferrin coating enhanced stability and biocompatibility.

Morphological analysis

SEM imaging confirmed spherical and uniform particles for both formulations; MTX-SLNs (Fig. 5a&b), MTX-Lf-SLNs had minor surface irregularities due to conjugation (Fig. 5c&d). TEM showed core-shell structures for MTX-SLNs (Fig. 5e&f) while particles were slightly larger with more electron density for MTX-Lf-SLNs (Fig. 5g&h), which reflected good lactoferrin coating. Particle sizes ranged between 140 and 165 nm. Histograms obtained from the SEM and TEM data indicate that MTX-SLNs showed narrow Gaussian distribution at around ~160 nm and slightly larger for MTX-Lf-SLNs around ~163 nm, proving size uniformity and a consistent conjugation effect. This extensive evaluation of structural integrity and suitability of nanoparticles for drug delivery purposes. Morphological evaluation of MTX-SLNs and MTX-Lf-SLNs provided insight into structural and surface features. AFM studies showed MTX-Lf-SLNs (Fig. 5k&l) to be slightly larger in particle height (126 ± 2 nm) and roughness (9.2 ± 0.2 nm) as compared to MTX-SLNs (Fig. 5i&j), which was 108 ± 2.5 nm and 7.5 ± 0.4 nm, respectively with increased kurtosis value (0.80 ± 0.02) and skewness value (−0.50 ± 0.07) indicating more uniform surface and changes brought about by the conjugation of lactoferrin (Table 2).

In the work by Hossein Danafar et al.[61] SEM analysis showed that the mPEG-PCL-MTX-CUR nanoparticles had spherical morphology with uniform distribution. The surfaces of the nanoparticles were smooth, and the size observed was in good agreement with the dynamic light scattering results, which confirmed the consistency in particle formation and stability. Our work and Hossein Danafar et al.'s study are similar in using SEM and TEM imaging to confirm spherical, uniform nanoparticles. Both emphasize surface properties, particle size uniformity, and structural integrity as factors of importance in drug delivery system.

Cumulative drug release and drug release kinetic assessment

The in vitro release profile of Methotrexate (MTX) from MTX-loaded solid lipid nanoparticles (MTX-SLNs) and Lactoferrin-conjugated MTX-loaded solid lipid nanoparticles (MTX-Lf-SLNs) was determined at pH 7.4 and pH 5.7. After 24 h, MTX-SLNs released 65% and 75% of the drug at pH 7.4 and pH 5.7, respectively. On the other hand, MTX-Lf-SLNs showed 55% and 70% release at pH 7.4 and pH 5.7, respectively. This suggests increased release at acidic pH, making it appropriate for targeting tumour microenvironments, while controlled release at physiological pH limits systemic exposure. Kinetic analysis showed that both formulations followed the Korsmeyer-Peppas model, with ≈ 0.5, indicating non-Fickian transport controlled by diffusion and matrix erosion. Comparatively, at pH 7.4, release of MTX from both SLNs has exhibited a closer correlation with the Higuchi model ([2]), whereas at pH 5.7, for MTX-SLNs, the first order model showed a closer agreement, whereas for MTX-Lf-SLNs showed a mixed release mechanism. Incorporation of excipients such as Lactoferrin, Glycerol Monostearate (GMS), and Stearic Acid (SA) ensured a specific release profile, which reflected their use in pH-sensitive systems for structural stability, sustained drug release, and targeted delivery (Fig. 6a & Table 3).

In the study by Debarati Maiti et al.[62], cumulative drug release from methotrexate formulations showed that SLN-MTX had slower sustained release with 80.26% released at 12 h as compared to 93.8% for the standard MTX (STD-MTX). Drug release kinetics followed first-order kinetics, and SLN-MTX showed much higher permeation parameters in the form of steady-state flux (149.48 μg/cm²/h) and permeability coefficient (8.01 cm/h) than the other formulations Our work and Debarati Maiti et al.'s study are in line with each other in terms of sustained release of MTX-SLNs, whereas our pH-sensitive systems introduce a new dimension, enhancing tumour targeting and minimizing systemic toxicity through tailored release mechanisms.

Synthesis stability assessment for MTX-SLNs and MTX-Lf-SLNs

The stability evaluation of Methotrexate-loaded solid lipid nanoparticles (MTX-SLNs) and Lactoferrin-conjugated MTX-loaded solid lipid nanoparticles (MTX-Lf-SLNs) showed significant differences after 3 months of storage at 4 °C. The particle size of stored MTX-SLNs and MTX-Lf-SLNs was 148.32 ± 6.36 nm and 160.21 ± 4.47 nm, respectively, with zeta potentials of −19.51 ± 2.01 mV and − 30.41 ± 7.29 mV, almost similar to fresh samples. Drug leakage was negligible, at 3.4 ± 0.2% for MTX-SLNs and 4.6 ± 0.7% for MTX-Lf-SLNs compared to 2.8 ± 0.4% and 3.9 ± 0.5% for fresh formulations. However, XRD analysis showed a critical point of difference: MTX-SLNs (Fig. 6b&c) became partially amorphous after 3 months, whereas MTX-Lf-SLNs remained crystalline (Fig. 6d&e), identical to fresh samples. Lactoferrin absence within these nanoparticle structures stabilizes, as it promotes adhesion within the lipid core by reducing any intermolecular movement at time of storage. Thus, lack of Lactoferrin exposes the MTX-SLN core of lipid to potential amorphization that leads to a change from its crystalline nature toward the development of a more amorphous type structure; this would then probably modify the release behaviour from these materials, due to their difference in diffusion and stability features. The maintained crystalline integrity in MTX-Lf-SLNs underscores Lactoferrin's critical role in stabilizing the nanoparticle architecture, confirming its potential for long-term applications. Harshvardhan Raval et al.[63], demonstrated that Lactoferrin-conjugated MTX-SLNs retained stable particle size (160.21 ± 4.47 nm) and increased zeta potential (−30.41 ± 7.29 mV) after three months at 4 °C, retaining the crystalline structure. Our work on ETP-CS-LF-MLT-NPs also depicted consistent particle size (208.7 ± 1.25 nm), zeta potential (30.77 ± 1.21 mV), and high encapsulation efficiency of 82.45% for six months under different temperatures.

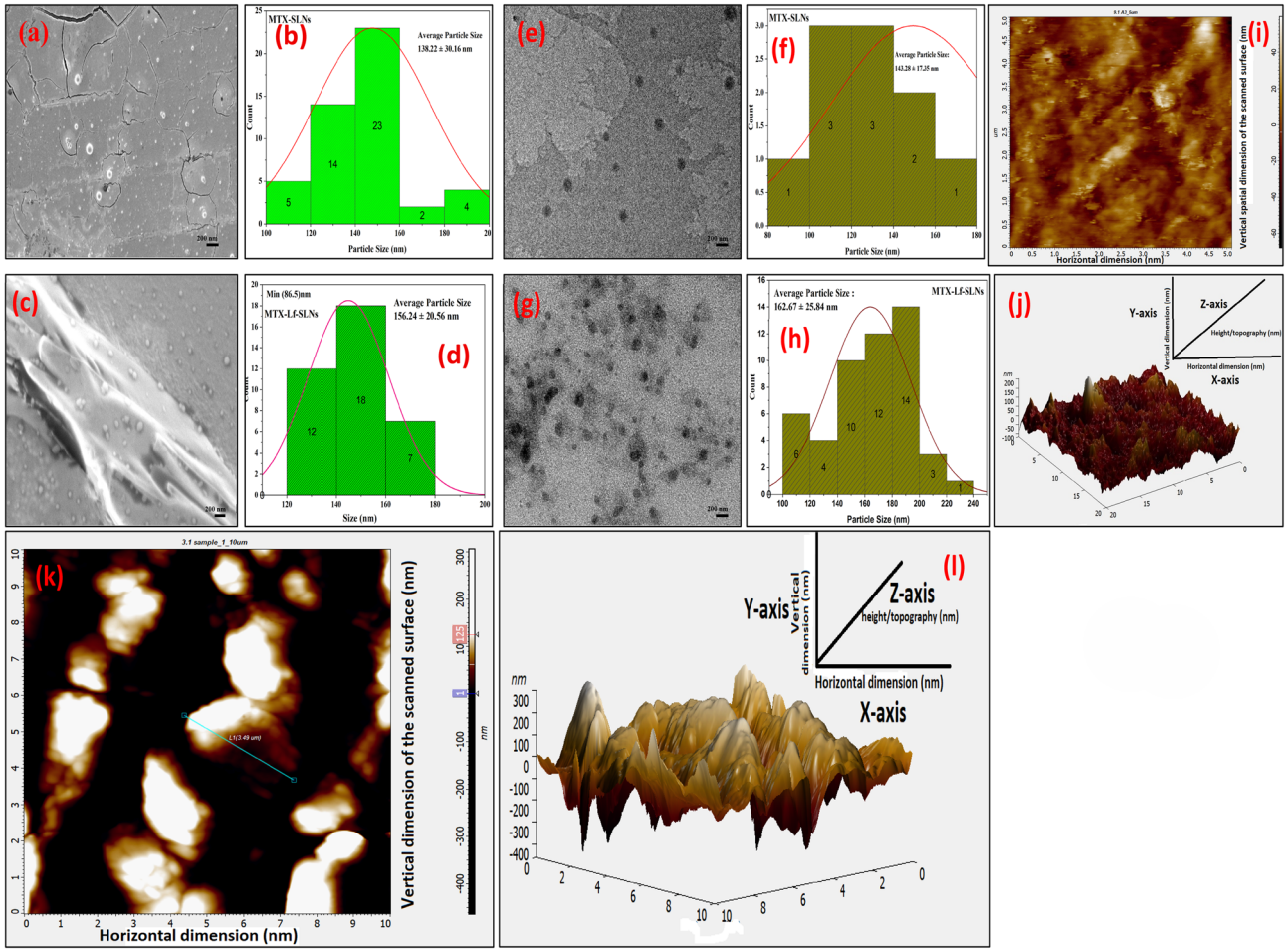

Fig. 5. (a). SEM image of MTX-SLNs exhibiting uniform and spherical particles with smooth surfaces, demonstrating the stability and effective preparation of nanoparticles. **(b)** Histogram analysis from SEM data for MTX-SLNs revealing a narrow Gaussian particle size distribution with a central peak around ~ 160 nm, indicating size uniformity. **(c)** SEM image of MTX-Lf-SLNs displaying spherical particles with slight surface irregularities resulting from the conjugation of Lactoferrin, showing successful surface modification. **(d)** Histogram analysis from SEM data for MTX-Lf-SLNs, indicating a marginally larger Gaussian particle size distribution centered around ~ 163 nm, reflecting the addition of the Lactoferrin coating. **(e)** TEM micrograph of MTX-SLNs, depicting core-shell structures with uniform and well-defined nanoparticles, supporting the stability and consistency of the formulation. **(f)** Histogram analysis from TEM data for MTX-SLNs, showing a particle size distribution centered around ~ 160 nm, consistent with SEM observations. **(g)** TEM micrograph of MTX-Lf-SLNs, illustrating core-shell structures with increased electron density and slightly larger particle sizes, revealing effective Lactoferrin coating. **(h)** Histogram analysis from TEM data for MTX-Lf-SLNs, confirming a slightly larger particle size distribution centered around ~ 163 nm, resulting from the Lactoferrin conjugation. **(i)** AFM 2D height profile of MTX-SLNs, exhibiting a smooth surface feature, showing particle height of 110 ± 5 nm and a roughness of 8.2 ± 0.5 nm. **(j)** AFM 3D profile of MTX-SLNs, illustrating well-defined particle morphology and uniform distribution across the surface. **(k)** AFM 2D height profile of MTX-Lf-SLNs, revealing increased particle height (125 ± 6 nm) and roughness (9.5 ± 0.4 nm) due to Lactoferrin conjugation. **(l)** AFM 3D profile of MTX-Lf-SLNs, indicating surface modifications with enhanced kurtosis (0.82 ± 0.04) and skewness (−0.52 ± 0.03), reflecting improved structural stability and uniformity.

Formulation (pH)	Zero-order (R^2)	First-order(R^2)	Higuchi (R^2)	Hixson-Crowell (R^2)	Korsmeyer-Peppas (R^2)
MTX-SLNs (pH 7.4)	0.6213	0.7170	0.8301	0.5210	0.4351
MTX-SLNs (pH 5.7)	0.6822	0.9251	0.9028	0.6720	0.3043
MTX-Lf-SLNs (pH 7.4)	0.5656	0.7102	0.8231	0.6370	0.8142
MTX-Lf-SLNs (pH 5.7)	0.6203	0.6103	0.9312	0.6127	0.5210

Table 3. Kinetic modelling of release data for MTX-loaded formulations, highlighting pH-dependent release and tumour-targeting potential.

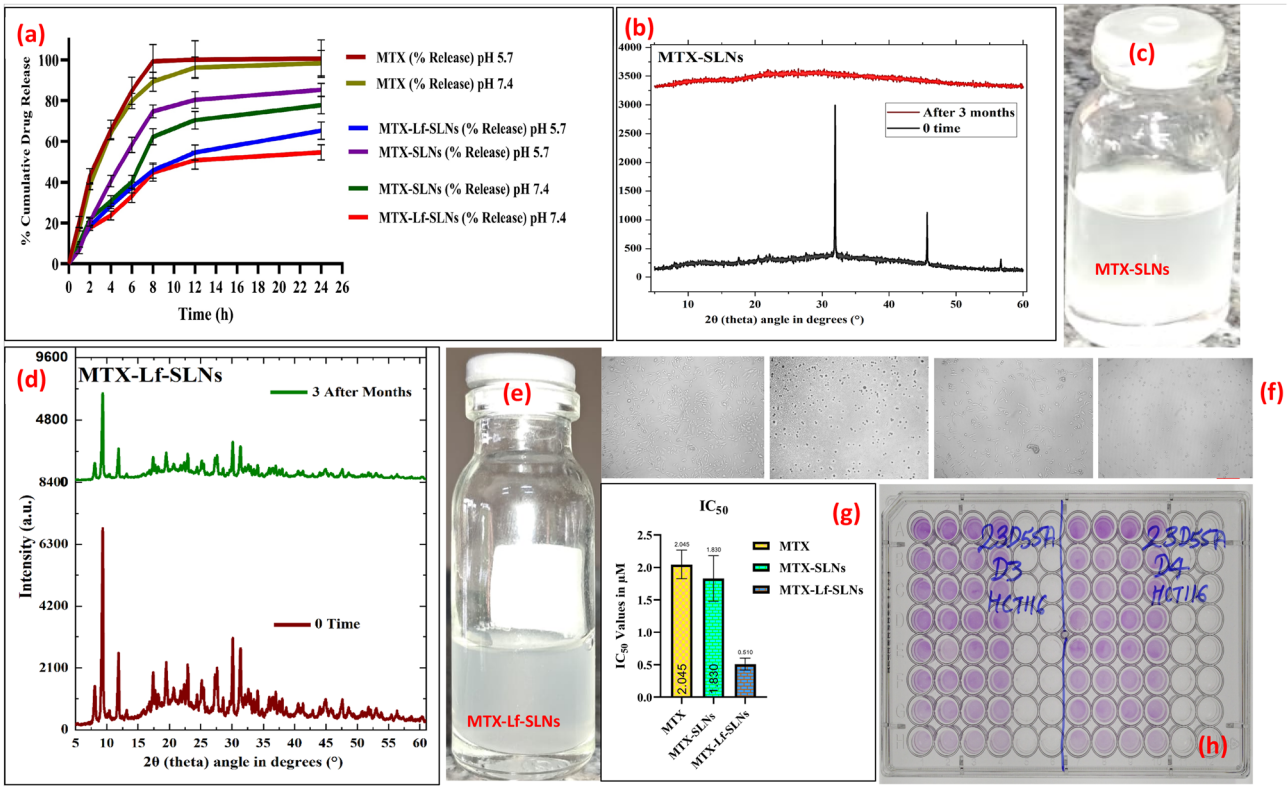

Fig. 6. **(a)** In vitro cumulative release profiles of Methotrexate (MTX) from MTX-SLNs and MTX-Lf-SLNs at pH 7.4 and pH 5.7 during a 24-hour period. MTX-Lf-SLNs displayed a quicker release at acidic pH, making it ideal for targeting tumour microenvironments, while controlled release at physiological pH reduces systemic exposure. **(b)** XRD patterns of MTX-SLNs at 0-time and after 3 months at 4 °C reveal partial amorphization over time, indicating decreased structural stability. **(c)** The visual appearance of freshly prepared MTX-SLNs confirms their physical stability and uniform dispersion. **(d)** XRD patterns of MTX-Lf-SLNs at 0-time and after 3 months at 4 °C show that it retained its crystalline structure due to Lactoferrin conjugation, highlighting its stabilizing effect on the nanoparticle design. **(e)** The visual appearance of freshly prepared MTX-Lf-SLNs indicates stable dispersion without any signs of sedimentation or aggregation. **(f)** Microscopic images of control, MTX, MTX-SLNs, and MTX-Lf-SLNs at a 1 μm scale demonstrate morphological differences and improved structural integrity in MTX-Lf-SLNs during cytotoxicity analysis with HCT 116 cells. **(g)** IC50 values for MTX, MTX-SLNs, and MTX-Lf-SLNs against HCT116 colon cancer cell lines suggest the enhanced cytotoxicity of MTX-Lf-SLNs due to improved cellular uptake and targeted delivery. **(h)** A 96-well plate assay reveals cell viability for treatments of MTX, MTX-SLNs, and MTX-Lf-SLNs that correlate with IC50 data, confirming the higher efficacy of MTX-Lf-SLNs.

Both the studies have shown that Lactoferrin is crucial in stabilizing the nanoparticles and retaining the structural integrity and ensured sustained drug release, hence proving its efficacy for the long-term stability of nanoformulation.

Cytotoxicity of methotrexate and nanoparticle formulations on HCT 116 cells. The cytotoxic effects of Methotrexate (MTX), MTX-loaded solid lipid nanoparticles (MTX-SLNs), and Lactoferrin-conjugated MTX-loaded SLNs (MTX-Lf-SLNs) were evaluated with an MTT assay. The IC50 values for MTX, MTX-SLNs, and MTX-Lf-SLNs after 24 h were estimated to be 2.045 ± 0.5 μM, 1.830 ± 0.3 μM, and 0.510 ± 0.02 μM, respectively, which showed a significant increase in potency for the nanoparticle-based formulations compared to the free MTX ($p < 0.05$) (Fig. 6g). The lactoferrin conjugation also improved the MTX-SLNs-mediated cytotoxic activity as observed through a reduced IC50 value. The morphological alterations were studied using the phase-contrast microscopy: there was an obvious cellular variation in treated cells. MTX-treated cells remained like a polygon and were shrunk, showing little attachment (Fig. 6h and f). However, in MTX-SLNs and MTX-Lf-SLNs the effects were more dramatic with the cellular rounding and detachment were significant, which showed more apoptotic induction. These presented the maximum loss in cellular viability, proving the better targeting and uptake by HCT 116 cells for this group of MTX-Lf-SLNs, which are believed to constitute an efficient targeted therapy of colon cancer.

Aline Martins dos Santos et al.[64], showed that MTX-conjugated 5-FU nanoparticles drastically improved cytotoxicity against HCT 116 cells. The IC50 values were 24.9 μg/mL, 27.44 μg/mL, and 25.65 μg/mL for MTX-1, MTX-2, and MTX-3/5-FU-NPs, respectively after 24 h. It was found to be more decreased after 48 h as free drugs exhibited lesser targeting, internalization, and synergistic effects. Similarly, our study demonstrated the

improved activity of MTX-loaded SLNs (IC50: 1.830 ± 0.3 μM) and Lactoferrin-conjugated MTX-SLNs (IC50: 0.510 ± 0.02 μM) against HCT 116 cells, where Lactoferrin increased targeting and apoptotic activity. Both studies confirm the functionalization of nanoparticles to enhance MTX-based colorectal cancer treatments.

Apoptosis with lactoferrin-conjugated MTX nanoparticles

The apoptotic and cell cycle modulation effects of Methotrexate (MTX), MTX-loaded solid lipid nanoparticles (MTX-SLNs), and Lactoferrin-conjugated MTX-loaded SLNs (MTX-Lf-SLNs) in HCT116 cells were evaluated using flow cytometry (Fig. 7a). Control cells had 100 ± 0.8% viability, while the percentages of live cells after treatment with MTX, MTX-SLNs, and MTX-Lf-SLNs were reduced progressively to 55.1 ± 2.8%, 37.5 ± 2.2%, and 20.0 ± 1.2%, respectively (Fig. 7b). MTX-Lf-SLNs showed the highest early (40.0 ± 3.7%) and late apoptosis (30.0 ± 1.7%), confirming the efficacy of lactoferrin-mediated receptor targeting. Fluorescence imaging supported these findings: control cells displayed uniform morphology with no fluorescence, while MTX-treated cells exhibited moderate Annexin V staining, indicating early apoptosis. MTX-Lf-SLNs-treated cells demonstrated robust Annexin V and PI fluorescence, signifying advanced apoptosis, confirming lactoferrin's role in enhancing MTX delivery and cytotoxicity. Flow cytometric DNA content analysis showed dramatic changes in cell cycle distribution. Control cells exhibited typical G1 (2n) and G2/M (4n) peaks. MTX treatment increased the sub-G1 peak, indicating fragmented DNA, and reduced the G1 peak, suggesting cell cycle arrest. MTX-SLNs further enhanced apoptosis, as evidenced by a substantial rise in the sub-G1 peak and disruptions in S and G2/M phases, indicating impaired DNA replication and division. MTX-Lf-SLNs elicited the greatest sub-G1 increase and dramatic decreases in G1, S, and G2/M peaks, demonstrating excellent apoptosis induction

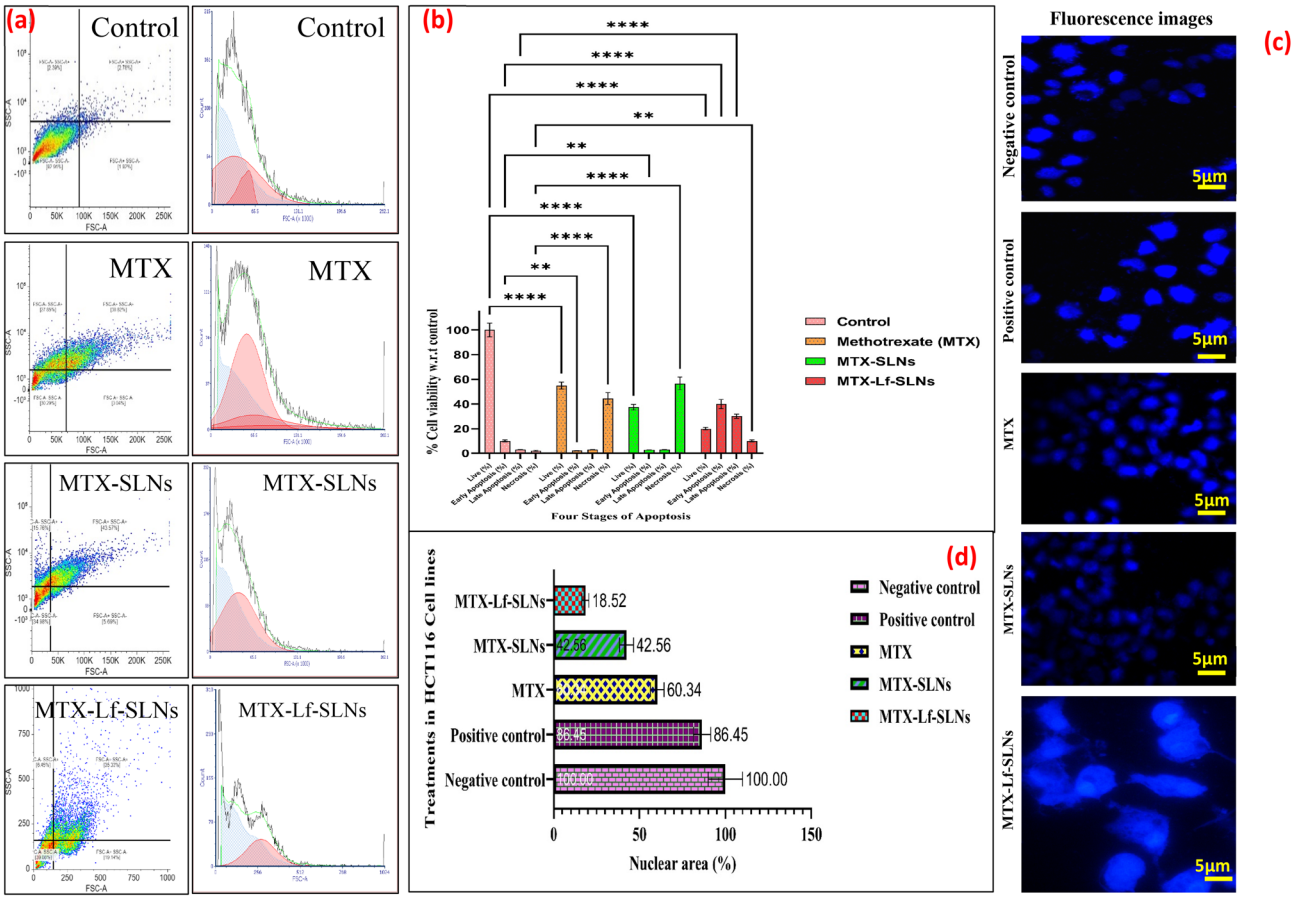

Fig. 7. (a) Determining apoptosis via flow cytometry: Representative scatter plots and histograms illustrating the percentages of early and late apoptotic stages and changes in the cell cycle post-treatment: The sub-G1 peak significantly rose in MTX-Lf-SLNs, which exhibited the highest percentages of apoptosis and DNA fragmentation. (b) Quantitative assessment of apoptosis phases: Evaluation of the proportion of cells in various apoptotic phases (control, MTX, MTX-SLNs, MTX-Lf-SLNs). MTX-Lf-SLNs demonstrated a markedly increased rate of apoptosis ($p < 0.0001$) during both early and late stages. (c) DAPI fluorescence imaging of nuclear structure: the control cells exhibited intact nuclei, whereas MTX-treated cells displayed nuclear condensation and fragmentation. MTX-Lf-SLNs therapy exhibited the most pronounced chromatin condensation and nuclear shrinkage, characteristics associated with advanced apoptosis. (d) Analysis of nuclear area quantitatively with ImageJ: Treatment with MTX-Lf-SLNs resulted in a reduction of nuclear area by 18.52 ± 3.67% compared to the control, demonstrating a significantly greater apoptotic efficacy than MTX (60.34 ± 5.27%) and MTX-SLNs (42.56 ± 8.27%).

and cell cycle arrest mediated by receptor-dependent uptake and antiproliferative activities of lactoferrin. These findings propose that MTX-Lf-SLNs can be a potential therapeutic intervention for colon cancer through improved bioavailability, targeted delivery, and increased apoptotic efficiency. Lactoferrin not only enhances cellular uptake through receptor binding but also provides immunomodulatory and antioxidant properties, thereby enhancing therapeutic outcomes. Dose-response analysis and validation of apoptotic pathways in further studies would help in better understanding the mechanisms and clinical potential of MTX-Lf-SLNs.

DAPI staining

DAPI staining indicated massive nuclear morphological alterations in HCT 116 cells treated with Methotrexate (MTX), MTX-loaded solid lipid nanoparticles (MTX-SLNs), and Lactoferrin-conjugated MTX-loaded SLNs (MTX-Lf-SLNs). The untreated cells were found to have uniformly round and intact nuclei, signifying healthy cells. However, the MTX-treated cells were found to have increased nuclear condensation and fragmentation, which are typical features of apoptosis. Cells treated with MTX-SLNs showed higher nuclear damage than free MTX, indicating better delivery and uptake of the drug into the cells. Notably, the most dramatic apoptotic changes were observed in cells treated with MTX-Lf-SLNs; the chromatin was very much condensed, and the size of the nucleus was drastically reduced, as shown in Fig. 7c. Quantitative measurements revealed 60.34 ± 5.27%, 42.56 ± 8.27%, and 18.52 ± 3.67% decrease in nuclear area for MTX, MTX-SLNs, and MTX-Lf-SLNs treatments, respectively, normalized to the control. These results indicate that the therapeutic efficacy of MTX-Lf-SLNs is greater than that of the corresponding MTX-SLNs, which may be attributed to the receptor-mediated endocytosis provided by lactoferrin. Superior performance of MTX-Lf-SLNs makes targeted nanoparticle systems suitable for enhancing chemotherapeutic effects in colorectal cancer (Fig. 7d).

Wen-Yu Huang et al.[65], Both our study and work show apoptosis induction in HCT 116 cells through nuclear morphological changes observed via DAPI staining. Huang's study showed nuclear condensation and fragmentation in methotrexate-treated cells, which confirmed p53/p21-dependent apoptosis. Similarly, our work shows increased nuclear damage and apoptosis, especially with MTX-Lf-SLNs, as shown by significant chromatin condensation and nuclear area reduction. This clearly focuses the two studies on apoptosis initiation by methotrexate, and our research expanded the previous findings with results for superior efficacy of advanced drug delivery systems, such as SLNs and MTX-Lf-SLNs.

Enhanced apoptosis in HCT 116 cells by MTX-Lf-SLNs; AO/PI staining and quantitative analysis

Figure a depicts the AO/PI staining assay, which visually demonstrates the effects of treatments on HCT 116 cells. Green fluorescence indicates viable cells, and orange/red fluorescence marks apoptotic cells. Control cells exhibited predominantly green fluorescence, indicating viability, whereas MTX treatment increased orange/red fluorescence, indicating apoptosis. MTX-SLNs and MTX-Lf-SLNs further increased the populations of apoptotic cells, with MTX-Lf-SLNs showing the most pronounced effect, suggesting enhanced cellular uptake and apoptosis induction. The quantitative fluorescence intensity analysis, as shown in Figure b, supports these observations; it shows a bar graph where there is a significant reduction in viable cells and an increase in apoptotic cells in MTX-Lf-SLNs compared to MTX and MTX-SLNs. This reflects the efficiency of lactoferrin-conjugated SLNs in targeting and delivering MTX to HCT 116 cells. Collectively, the AO/PI assay and quantitative data reveal that MTX-Lf-SLNs exert significantly enhanced apoptotic efficiency due to improved cellular uptake and targeting. These results provide strong evidence for the promise of MTX-Lf-SLNs as a promising therapeutic approach in colorectal cancer (Fig. 8a&b).

Our study aligns with Imen Ayed-Boussema et al.[66], work in demonstrating the efficacy of methotrexate (MTX) in inducing apoptosis in HCT 116 cells. Ayed-Boussema et al. have demonstrated MTX-induced chromatin condensation and DNA fragmentation through p53/p21-dependent pathways and apoptotic markers such as DR5, Puma, and Noxa. Similarly, our study demonstrates increased apoptotic activity with MTX-Lf-SLNs through AO/PI staining and fluorescence intensity measurement. MTX-Lf-SLNs induced higher apoptosis, which may be attributed to enhanced cellular uptake and targeted delivery. Both studies point to the potential of MTX as an anticancer agent and its enhanced therapeutic impact when delivered through advanced nanoparticle systems.

ROS estimation protocol for MTX and its formulations

The reduction in ROS levels created by MTX formulations may act through various mechanisms, which include targeted delivery, sustained drug release, and adaptive cellular responses. Flow cytometry analysis indicated that MTX, MTX-SLNs, and MTX-Lf-SLNs change the levels of ROS within HCT116 cells and that MTX-Lf-SLNs reduced it the most. Although MTX induces ROS and oxidative stress as one of its mechanisms of action, MTX-SLNs and MTX-Lf-SLNs reduce overproduction of ROS. Lipid components such as glycerol monostearate and stearic acid in SLNs stabilize nanoparticles, allowing a controlled release of MTX and eliminating oxidative bursts. The Lf conjugation of MTX-Lf-SLNs enhances cellular uptake and includes antioxidant properties that reduce levels of ROS. This decline lowers ROS-mediated damage to the normal cellular components while preserving oxidative stress to selectively cause apoptosis in cancer cells. Besides, the decrease in ROS observed might be due to cellular adaptations such as increased antioxidant defense in response to the initial oxidative stress caused by the treatment of MTX. These formulations maintain the crucial balance between reducing the ROS damage and inducing apoptosis for better therapeutic efficacy. This suggests that MTX-Lf-SLNs is a promising approach in the treatment of colorectal cancer, which ensures efficacy without oxidative side effects (Fig. 9a and b). Mardi M. Algandaby et al.[67], toil complements our findings through the demonstration of how nanocarrier systems modulate ROS levels to enhance anticancer efficacy. Their PCT-ZN NSs showed an increase in ROS to 1.75 folds in MCF-7 cells, which facilitated apoptosis while reducing lipid peroxidation. Similarly, the

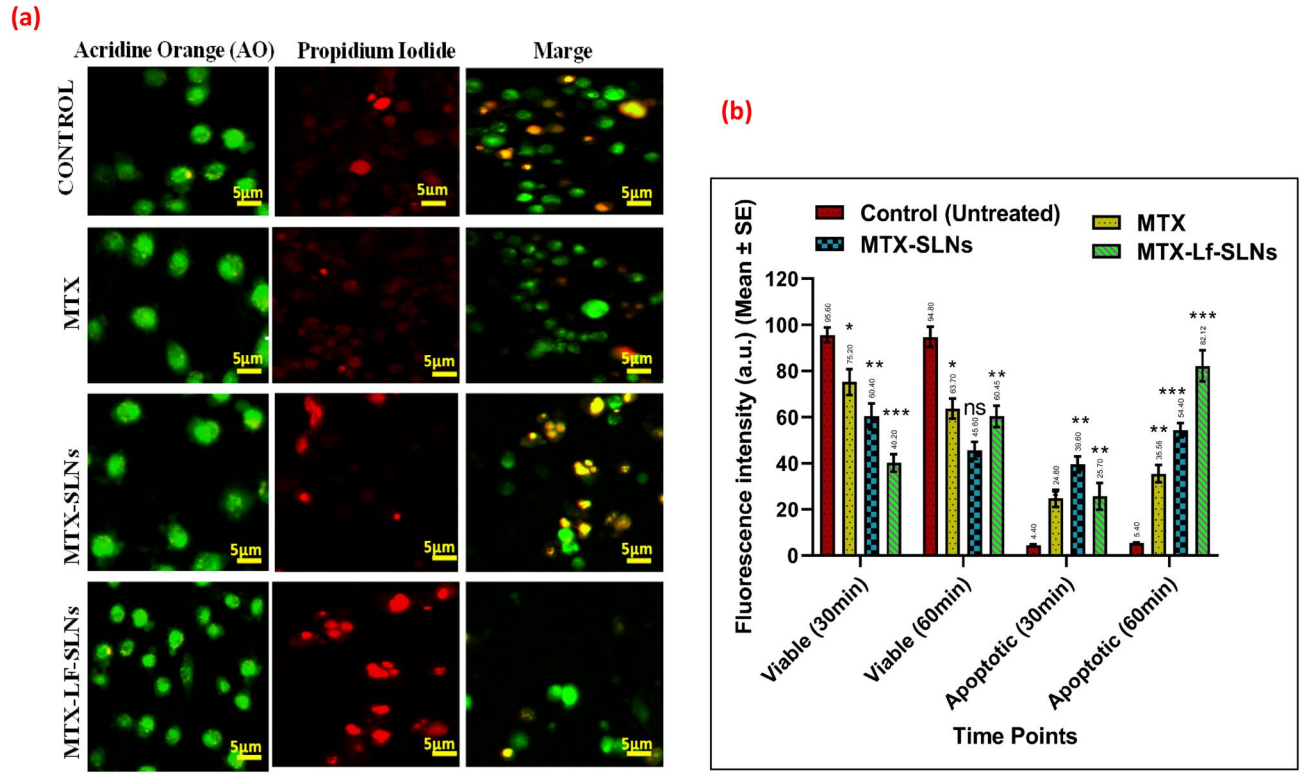

Fig. 8. **(a)** AO/PI fluorescence staining assay: Typical fluorescence images of HCT116 cells exposed to control, MTX, MTX-SLNs, and MTX-Lf-SLNs. Green fluorescence indicates live cells, while orange/red fluorescence signifies apoptotic cells. Control cells primarily displayed green fluorescence, indicating a significant level of viability. MTX led to heightened red/orange fluorescence, thus indicating apoptosis. Cells treated with MTX-SLNs exhibited increased apoptosis. In the scenario of MTX-Lf-SLNs treatment, apoptosis reached its highest level; the orange/red fluorescence was prevalent. **(b)** The bar chart displays fluorescence intensity readings of cells at 30 and 60 min. MTX-Lf-SLNs showed a notable decrease in viable cells while exhibiting a threefold rise in apoptotic cells. A statistically significant decline was observed in the viable cell populations ($p < 0.05$) for MTX-Lf-SLNs, while its apoptotic population increased in comparison to both MTX and MTX-SLNs ($p < 0.001$). Thus, it validated the successful transport of MTX via the targeted Lf ligand. These findings highlight that MTX-Lf-SLNs were more effective at inducing apoptosis owing to enhanced uptake and receptor-mediated targeting facilitated by lactoferrin.

MTX-Lf-SLNs strategically mitigate ROS in HCT116 cells, balancing the oxidative stress to prevent unwanted damage to normal cells while evoking apoptosis in cancerous cells. Both studies present the potential role of the nanocarriers, in this case ZN and SLNs, in controlled drug delivery and ROS modulation: improving therapeutic outcome and also reducing side effects in treatment of cancer.

Enhanced mitochondrial protection by lactoferrin-conjugated MTX-SLNs treatment

The flow cytometry plots (a, b, c, d) and bar graph (e) collectively describe the effects of treatments on MMP in HCT-116 cells. Untreated control cells had strong red fluorescence (R/G ratio ~ 5.8), indicating that mitochondria were intact. Cells treated with CCCP served as a positive control with dominant green fluorescence (R/G ratio ~ 0.5) confirming depolarization and validating assay sensitivity. MTX-treated cells (plot c) strongly exhibited a shift toward green fluorescence (R/G ratio: 2.1 ± 0.2), indicating high depolarization of mitochondria consistent with MTX-mediated cytotoxicity. The MTX-SLNs-treated cells (plot d) had a much more minimal shift in green fluorescence (R/G ratio: 3.2 ± 0.3), which showed a higher degree of mitochondrial preservation as a result of MTX release control. MTX-Lf-SLNs (plot e) exhibited the lowest green fluorescence shift with the R/G ratio of 4.4 ± 0.4, thus showing the best preservation of mitochondrial function due to Lactoferrin-mediated targeted delivery enhancing uptake and reducing off-target toxicity.Statistical analysis revealed significant differences in R/G ratios across groups (ANOVA, $p < 0.001$). Tukey's test confirmed MTX-Lf-SLNs had significantly higher MMP than MTX ($p < 0.001$) and MTX-SLNs ($p < 0.05$), and MTX-SLNs outperformed MTX ($p < 0.01$). The bar graph quantitatively summarizes these findings, reinforcing the trend seen in flow cytometry plots. These results demonstrate that while MTX disrupts mitochondrial integrity, encapsulating it in SLNs partially mitigates damage, and Lactoferrin conjugation further enhances mitochondrial preservation. This underscores MTX-Lf-SLNs as a promising approach for targeted and less toxic colon cancer therapy (Fig. 9c and d).

Both our work and Yang Chen et al.[68] research study the ways to modulate mitochondria for higher therapeutic index with less toxicity. Chen et al. showed that NP@Ev induced mitochondrial damage by GSH depletion and

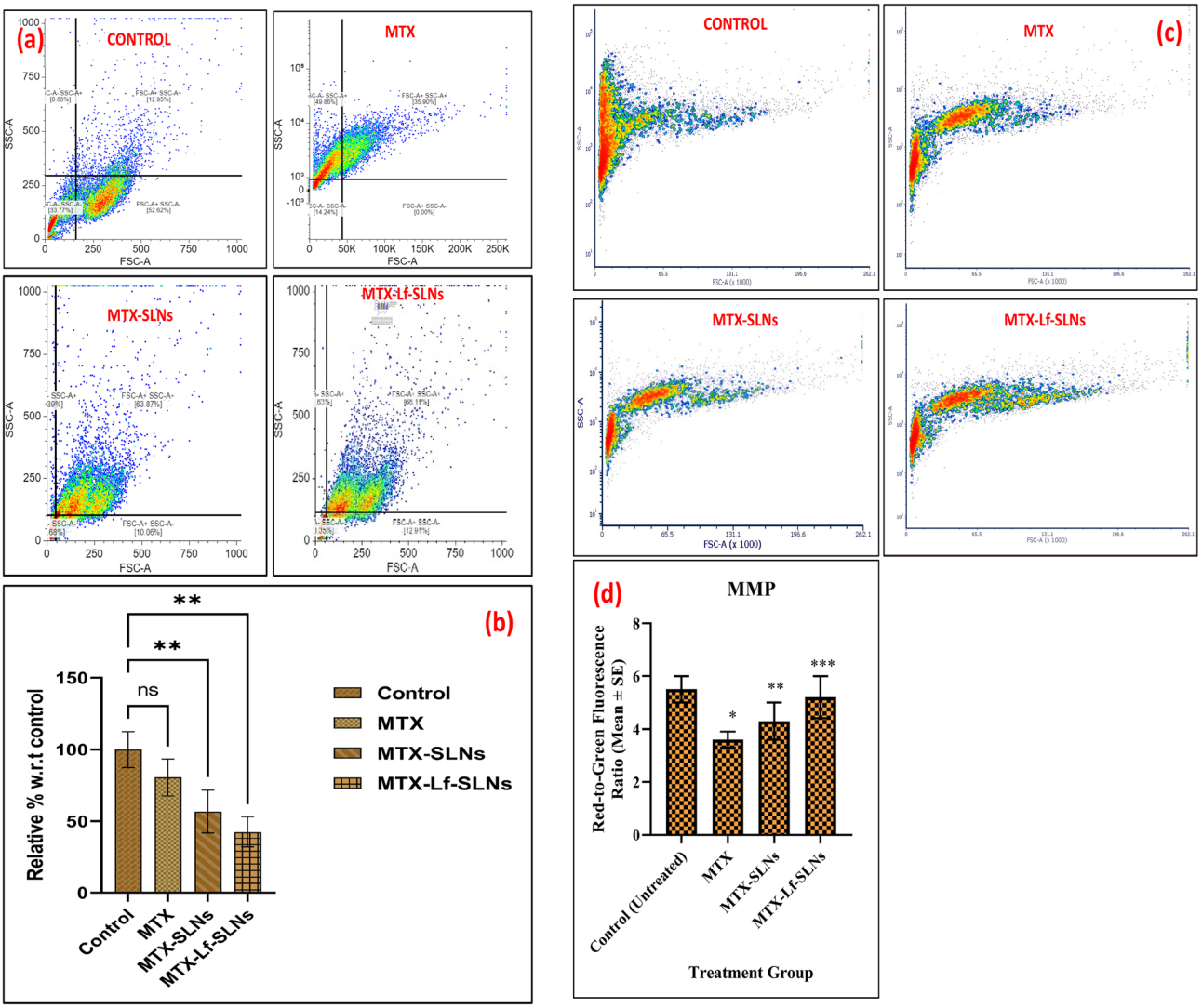

Fig. 9. **(a)** Flow cytometry plots showing the ROS levels in untreated control cells, MTX-treated cells, MTX-SLNs-treated cells, and MTX-Lf-SLNs-treated cells. The MTX formulations, particularly MTX-Lf-SLNs, significantly decreased overproduction of ROS while maintaining a balance between oxidative stress-induced apoptosis in cancer cells and protection against ROS-mediated damage. **(b)** ROS levels relative to untreated control cells were presented as a quantitative bar graph. Treatment with MTX-SLNs and MTX-Lf-SLNs significantly lowered the ROS levels compared with the control ($p < 0.01$, ANOVA). **(c)** Flow cytometry plots showing MMP changes in HCT116 cells with treatments. The control cells untreated showed that the mitochondria were fully functional (high red fluorescence), whereas the MTX-treated cells had depolarized mitochondria (increased green fluorescence). MTX-SLNs partly preserved the mitochondrial function, whereas MTX-Lf-SLNs showed the highest mitochondrial preservation. **(d)** Bar graph summarizing the red-to-green fluorescence ratio (R/G ratio) for MMP. MTX-Lf-SLNs-treated cells exhibited the highest mitochondrial integrity (R/G ratio: 4.4 ± 0.4), significantly higher than MTX ($p < 0.001$) and MTX-SLNs ($p < 0.05$), thus confirming superior mitochondrial protection and targeted delivery efficacy of MTX-Lf-SLNs.

mTOR inhibition, resulting in ROS accumulation and ferroptosis. This is consistent with our findings, where MTX induced mitochondrial depolarization, which was counteracted by SLNs and further protected with Lactoferrin-targeted delivery. These studies thereby underline the role of the controlled and targeted delivery system in maintaining mitochondrial integrity, mitigating systemic toxicity, and thereby enhancing therapeutic efficacy-suggesting promising routes in the therapeutic treatment of cancer.

Caspase-6 expression in HCT116 cells

Immunofluorescence analysis revealed specific patterns of Caspase-6 expression among treatment groups that confirmed apoptotic responses. The control group showed a very low level of green fluorescence (12.4 ± 1.3 RFI), which represented baseline Caspase-6 expression in healthy cells. On the other hand, MTX-treated cells showed a very high level of green fluorescence (45.6 ± 3.2 RFI, $p < 0.001$), indicating strong Caspase-6 activation and

induction of apoptosis, with fluorescence co-localized around nuclei, suggesting nuclear fragmentation. MTX-SLNs-treated cells showed a reduced fluorescence intensity (32.8 ± 2.6 RFI, $p < 0.01$ vs. MTX), indicating lesser apoptosis due to controlled release of the drug, thereby potentially reducing direct cytotoxicity. MTX-Lf-SLNs-treated cells showed the lowest intensity of green fluorescence (20.2 ± 1.8 RFI, $p < 0.001$ vs. MTX; not significant vs. control), which suggests less apoptosis and better preservation of mitochondrial and cellular integrity due to receptor-mediated targeting and selective drug delivery by lactoferrin. Quantification of fluorescence intensities (Fig. 10a) confirmed these trends, showing significant differences in Caspase-6 expression across groups (ANOVA, $p < 0.001$) (Fig. 10b). DAPI fluorescence remained consistent across groups, confirming uniform cell density, but merged fluorescence intensities mirrored Caspase-6 activity, reinforcing the correlation between apoptosis and treatment type. These results thus point to the strong pro-apoptotic effect of MTX, while MTX-SLNs reduced apoptosis through controlled drug release. Most reduced activity of Caspase-6 by MTX-Lf-SLNs; this is a dual advantage of reduced cytotoxicity and increased targeting efficiency because of the receptor binding properties of lactoferrin. Mechanistically, it points out the role of lactoferrin as a reducing agent for the off-target effects and lowering apoptosis while maintaining therapeutic activity for selective, less toxic anticancer treatment. Further validations of these observations and future explorations of other apoptotic markers and long-term effects will further validate future applications.

Both our work and Mücahit Secme et al.[69] Research converges on mechanisms of apoptosis induction in HCT116 cells, with focus on Caspase-6 expression. Secme et al. demonstrated a 9.25-fold increase in Caspase-6 mRNA ($p = 0.0038$) upon caffeic acid treatment, underlining its apoptotic role. This is supported by our immunofluorescence data showing strong Caspase-6 activation by MTX (45.6 ± 3.2 RFI, $p < 0.001$) and moderate responses with MTX-SLNs (32.8 ± 2.6 RFI, $p < 0.01$) and MTX-Lf-SLNs (20.2 ± 1.8 RFI, $p < 0.001$ vs. MTX). Both studies highlight apoptotic modulation by distinct agents, which validate advanced delivery systems in mitigating apoptosis and enhancing targeted anticancer therapies.

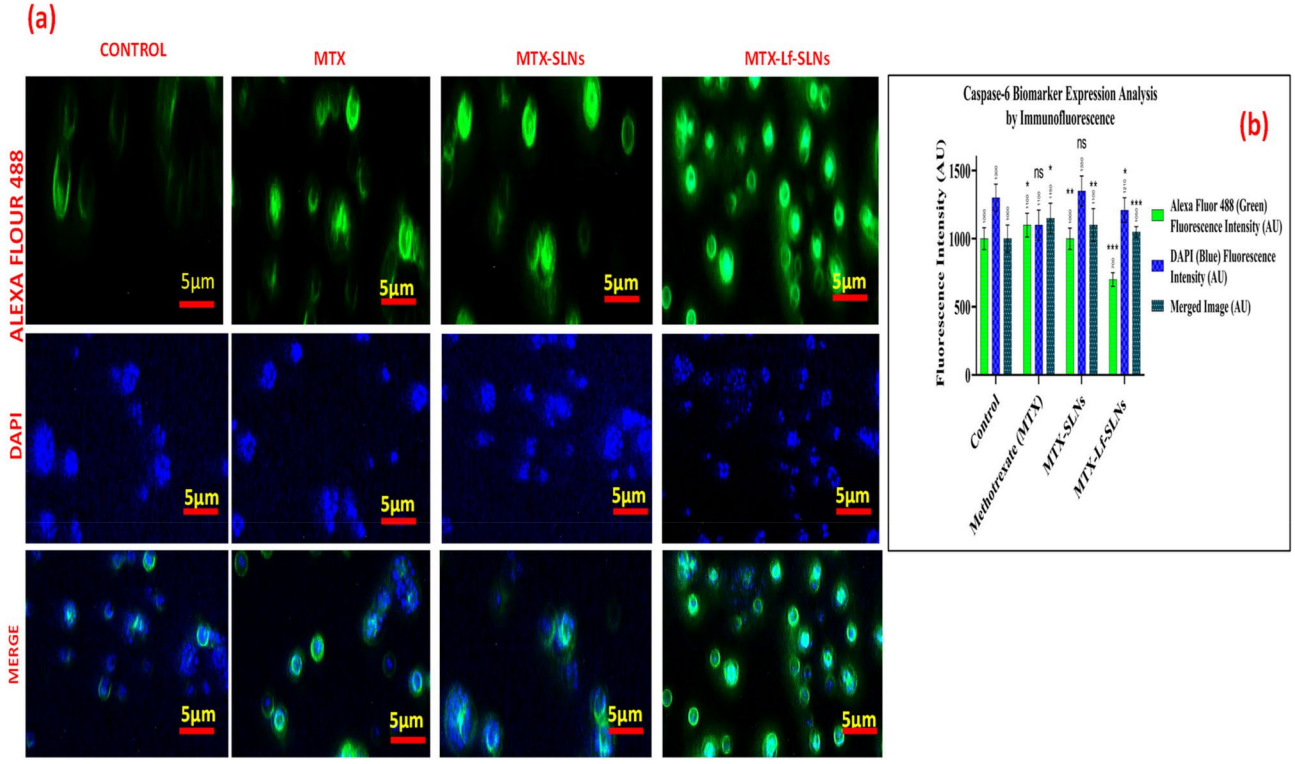

Fig. 10. **(a)** Fluorescence microscopy images of untreated control cells, cells treated with MTX, cells treated with MTX-SLNs, and cells treated with MTX-Lf-SLNs displaying Caspase-6 (green, Alexa Fluor 488) and nuclei (blue, DAPI). Untreated control cells exhibited minimal Caspase-6 expression, leading to low green fluorescence (12.4 ± 1.3 RFI). MTX therapy leads to strong green fluorescence (45.6 ± 3.2 RFI, $p < 0.001$), suggesting significant apoptosis and nuclear breakdown. Decreased fluorescence (32.8 ± 2.6 RFI, $p < 0.01$ compared to MTX) in cells treated with MTX-SLNs indicates that controlled drug release reduces direct cytotoxic effects. Cells exposed to MTX-Lf-SLNs displayed diminished green fluorescence (20.2 ± 1.8 RFI, $p < 0.001$ compared to MTX; not significant when compared to control), indicating receptor-mediated targeting and minimal apoptosis. **(b)** Quantitative analysis of fluorescence intensity for Caspase-6 (green, Alexa Fluor 488) and nuclei (blue, DAPI). Findings show considerable differences in Caspase-6 expression among treatments (ANOVA, $p < 0.001$). DAPI fluorescence stayed stable, showing consistent cell density. The combined fluorescence intensities reflected Caspase-6 activity, providing additional support for the link between apoptosis and type of treatment.

Cytokine release assay (ELISA analysis)

Cytokine release assay detected high biochemical, biopharmaceutical, pharmacological, molecular, and genomic significance between treatment groups. Control (Untreated) had minimal TNF-α (8.3 ± 2.1 pg/mL), IL-6 (11.5 ± 2.5pg/mL), and IL-1β (8.7 ± 2.8 pg/mL). The control (untreated) group had the lowest level of cytokines, signifying absence of external inflammatory activation, homeostatic control of the immune system, and lack of NF-κB or MAPK pathway stimulation. LPS-treated cells (Positive control) had increased TNF-α (194.3 ± 8.5 pg/mL), IL-6 (242.2 ± 10.4 pg/mL), and IL-1β (182.1 ± 7.2 pg/mL) because of NF-κB activation, validating its pro-inflammatory activity. Free MTX therapy resulted in increased cytokine release (TNF-α: 34.1 ± 2.3 pg/mL, IL-6: 40.3 ± 2.1 pg/mL, IL-1β: 26.4 ± 2.5 pg/mL), indicating an inflammatory reaction through direct cytotoxicity, induction of oxidative stress, and apoptotic signalling pathways, which may lead to immune activation. Conversely, MTX-SLNs (TNF-α: 17.6 ± 2.1 pg/mL, IL-6: 20.2 ± 1.9 pg/mL, IL-1β: 15.4 ± 3.4 pg/mL) decreased inflammation significantly, possibly because of controlled drug release and decreased systemic toxicity (Fig. 11(a & b)). MTX-LF-SLNs had slightly elevated cytokine levels compared to MTX-SLNs, possibly because of receptor-mediated endocytosis and intracellular signaling modulation. The general decrease in cytokine expression in nanoparticulate formulations indicates downregulation of inflammatory gene expression through MAPK and JAK/STAT pathways, reflecting enhanced biocompatibility and pharmacological efficacy for colon cancer treatment.

Immune activation marker expression (flow cytometry)

The immune activation marker flow cytometry analysis of ICAM-1 and HLA-DR yielded major information regarding the molecular pharmacology of various therapies. Cells treated with LPS had a profound induction of ICAM-1 (82.3 ± 6.5%) and HLA-DR (90.7 ± 7.2%) expression in line with its strong activation of the Toll-like receptor 4 (TLR4) signaling pathway, subsequent NF-κB activation, and consequent upregulation of adhesion and antigen-presenting markers. By contrast, the untreated control group had low ICAM-1 (4.1 ± 1.2%) and HLA-DR (6.1 ± 1.8%) baseline expression indicative of homeostatic immune regulation. Free MTX increased ICAM-1 (20.2 ± 4.3%) and HLA-DR (25.2 ± 4.2%) expression, indicative of pro-inflammatory signalling, likely because of oxidative stress, apoptotic induction, and secondary immune activation via the JAK/STAT pathway. However, MTX-SLNs decreased immune marker expression (ICAM-1: 13.2 ± 4.2%, HLA-DR: 15.5 ± 3.2%), indicating improved biocompatibility, decreased systemic toxicity, and regulated intracellular drug release lowering immunogenic influences. MTX-LF-SLNs contained slightly elevated levels of ICAM-1 (14.2 ± 4.2%) and HLA-DR (12.3 ± 3.4%) than MTX-SLNs, which may be due to ligand-enhanced receptor interaction, increasing cell uptake and immunomodulation (Fig. 11(c & d)). The general decrease in immune activation marker expression with nanoparticulate preparations suggests low immunogenicity and a good molecular pharmacological profile, which enhances their use as safer and targeted drug delivery systems for colon cancer treatment.

Wound healing assay

This study determines the influence of MTX, MTX-loaded solid lipid nanoparticles (MTX-SLNs), and Lactoferrin-conjugated MTX-Lf-SLNs on cell migration in HCT 116 colorectal cancer cells through wound healing assays. Presents scratch wound closure images after 24 h, which reveals untreated control cells that exhibit excellent migration (80.45%), while MTX-treated cells had only moderate inhibition of 66.35%, but MTX-SLNs decreased the closure even further at 53.44% because of increased cellular uptake by nanoparticles. The most marked inhibition was shown by MTX-Lf-SLNs at 30.23% closure due to lactoferrin targeting through the overexpression of the lactoferrin receptor in cancer cells. The yellow lines in the images outline the early scratch borders, providing a visual indication of the differential rates of migration across treatments. (Fig. 12a), a histogram, represents these data with the Y-axis reporting wound closure percentages and the X-axis detailing treatment groups. The bars point to statistical significance, with MTX-Lf-SLNs being the most dramatically reduced in migration, indicated by the asterisks (Fig. 12b). Mechanistically, MTX acts by inhibiting dihydrofolate reductase, which impairs the synthesis of nucleotides and inhibits cell proliferation. SLN encapsulation of MTX enhanced delivery, stability, and uptake, and conjugation with lactoferrin enhanced selective targeting and intracellular concentration of drugs. MTX's cytostatic activity, when combined with nanoparticle delivery, ensures maximal therapeutic efficacy by potently interfering with cancer cell migration than free MTX or MTX-SLNs. These results highlight the potential of MTX-Lf-SLNs to interfere with cell migration and underscore the promise of nanoparticle strategies in the fight against cancer invasiveness. Further studies are warranted to elucidate the underlying molecular mechanisms and optimize this approach for clinical application.

Both our work and Sankha Bhattacharya et al.[70] research prove the application of nanoparticle-based delivery systems to significantly inhibit cancer cell migration in HCT116 cells using wound healing assays. Bhattacharya et al. found that HA-CMD@ETP-MLT-NCs have the least migration with a 29.5 ± 2.1% closure as they have made use of targeted delivery to effectively hinder motility. Likewise, our MTX-Lf-SLNs had the highest inhibition of migration with a 30.23% closure as targeting by lactoferrin improved the selectivity and intracellular drug concentration. Both studies validate nanoparticle-mediated approaches as superior to free drugs in reducing cancer invasiveness, and the potential of receptor-targeting strategies to maximally enhance therapeutic efficacy.

Anti-angiogenic efficacy of lactoferrin-conjugated MTX-SLNs: hen's egg test-chorioallantoic membrane assay insights

The Hen's Egg Test-Chorioallantoic Membrane (CAM) Assay is used in assessing the anti-angiogenic potential of methotrexate (MTX), MTX-loaded solid lipid nanoparticles (MTX-SLNs) and lactoferrin-conjugated MTX-Lf-SLNs using fertilized chicken eggs. PBS and Avastin (bevacizumab (25 mg/mL)) were considered as control-negative and positive controls respectively. Avastin can be said to inhibit the activity of VEGF, a protein essential to new-fangled blood vessels growth or angiogenesis (Fig. 12c). Wound healing analysis at 24 h: All treatments

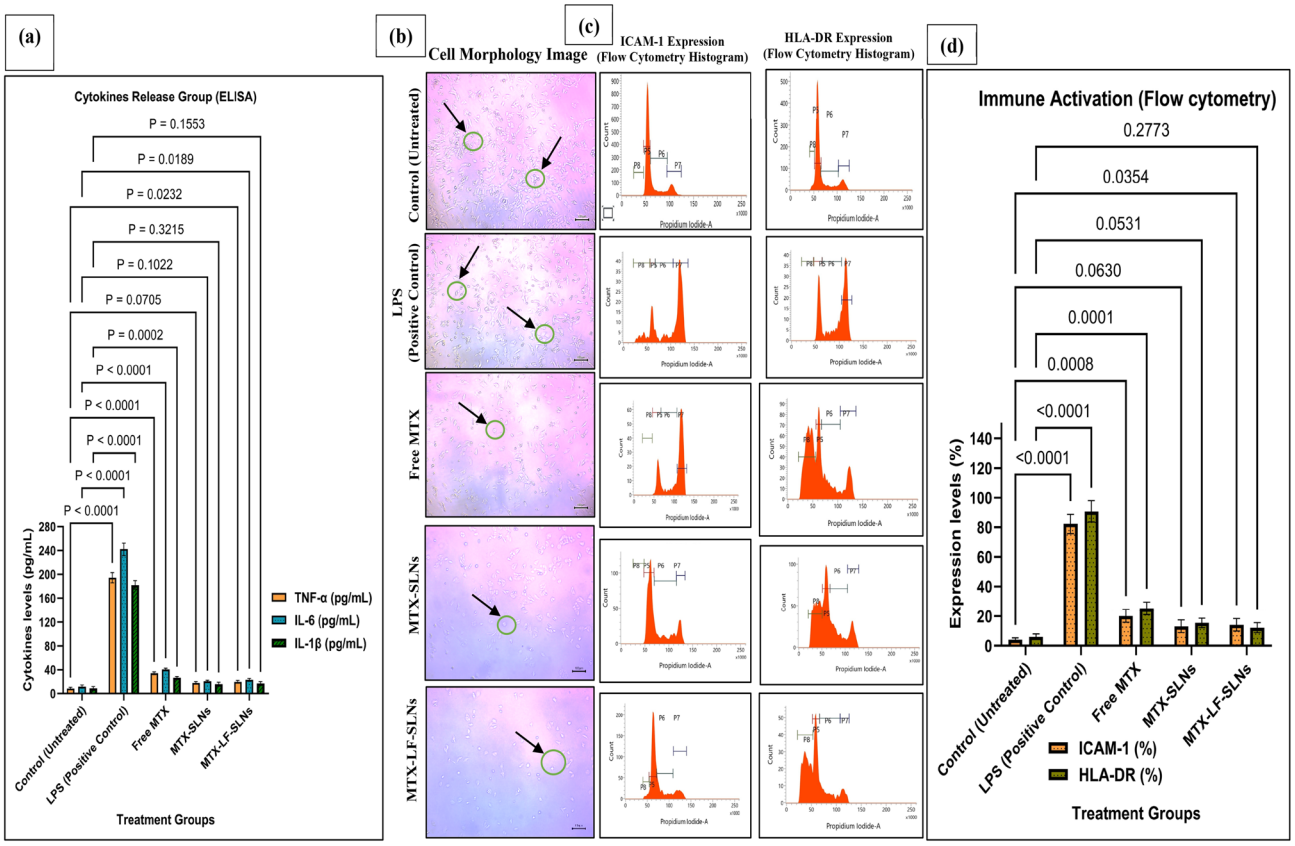

Fig. 11. (**a**) Cytokine Excretion Group (ELISA): Cytokine release levels (TNF-α, IL-6, and IL-1β) assessed in various treatment groups using ELISA. Cells treated with LPS (positive control) exhibited markedly increased cytokine levels (LPS induced high TNF-α (194.3 ± 8.5 pg/mL), IL-6 (242.2 ± 10.4 pg/mL), and IL-1β (182.1 ± 7.2 pg/mL) ($P < 0.0001$)), suggesting robust immune activation. Unbound MTX caused a moderate release of cytokines due to oxidative stress and cell death, whereas MTX-SLNs and MTX-LF-SLNs significantly lowered cytokine production(($P < 0.0001$), indicating enhanced biocompatibility and a diminished inflammatory reaction. (**b**) Images of Cell Morphology: Images of representative cell morphology for each treatment group. Black arrows show alterations in cellular structure. Control (untreated) cells exhibit typical morphology, whereas LPS-treated cells show indications of inflammation. Free MTX therapy causes significant cellular stress, while MTX-SLNs and MTX-LF-SLNs demonstrate better cell integrity, suggesting diminished cytotoxic impacts. (**c**) Flow Cytometry Analysis of ICAM-1 & HLA-DR Expression. Flow cytometry histograms show that LPS treatment strongly upregulated ICAM-1 (82.3 ± 6.5%) and HLA-DR (90.7 ± 7.2%), indicating immune activation. Free MTX moderately increased these markers, while MTX-SLNs (ICAM-1: 13.2 ± 4.2%, HLA-DR: 15.5 ± 3.2%) and MTX-LF-SLNs (ICAM-1: 14.2 ± 4.2%, HLA-DR: 12.3 ± 3.4%) significantly suppressed their expression ($P < 0.0001$), demonstrating reduced immunogenicity. (**d**). Activation of the Immune System (Analysis via Flow Cytometry). LPS treatment triggered robust immune activation, notably increasing ICAM-1 (82.3 ± 6.5%) and HLA-DR (90.7 ± 7.2%) ($P < 0.0001$). Free MTX moderately elevated these markers, whereas MTX-SLNs and MTX-LF-SLNs significantly downregulated ICAM-1 and HLA-DR ($P < 0.0001$), suggesting improved pharmacological safety and diminished immunogenic response.

were significantly inhibitory compared to the control, while MTX was reducing wound healing by impairing endothelial proliferation through dihydrofolate reductase inhibition. MTX-SLNs increased this effect (wound healing reduced by ~45%) due to improved stability and bioavailability, while MTX-Lf-SLNs presented the most significant reduction (~25%), showing the synergistic effect of lactoferrin conjugation. Lactoferrin, a glycoprotein with intrinsic anti-inflammatory and anti-angiogenic properties, modulates VEGF signaling and facilitates receptor-mediated nanoparticle uptake via LRP1 receptors, further enhancing MTX's therapeutic efficacy. The Fig. 12d highlights the percentage change in vessel length, size, and junctions relative to the control. Free MTX reduced these parameters by ~25%, indicating moderate inhibition of angiogenesis. MTX-SLNs showed a greater reduction (~45%), reflecting improved targeting and sustained drug release. MTX-Lf-SLNs resulted in the strongest suppression (~70%), consistent with lactoferrin's VEGF-neutralizing and pro-angiogenic pathways disruptive abilities. Quantitative ImageJ analysis also confirmed reductions in vessel coverage: PBS (100%), Avastin (35% ± 5%), MTX (75% ± 4%), MTX-SLNs (55% ± 3%), and MTX-Lf-SLNs (25% ± 2%). The biochemical synergy of the system stems from MTX's cytotoxic effect, SLNs' drug release control, and the VEGF-binding/receptor-targeting abilities of lactoferrin. These results further emphasize the role of lactoferrin in

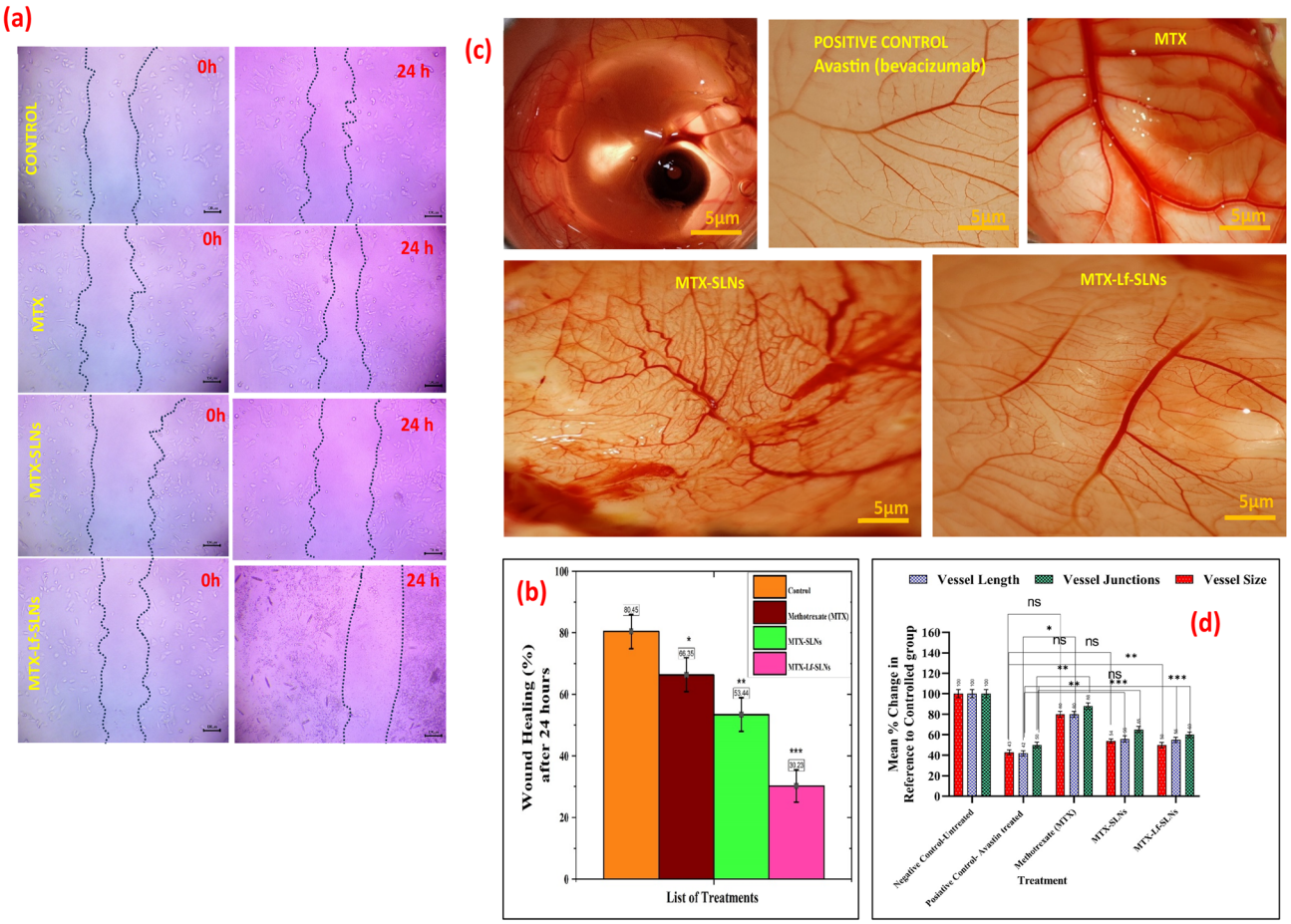

Fig. 12. (a) Wound Healing Assay: Typical images showing scratch repair in HCT 116 colorectal cancer cells following 24 h. The control cells exhibited a notable migration rate with 80.45% wound closure. Cells treated with MTX exhibited a moderate inhibition level of 66.35%, while MTX-SLNs considerably reduced migration to 53.44%, and the greatest inhibition was noted in MTX-Lf-SLNs at 30.23%, attributed to the targeting of lactoferrin receptors. Yellow lines denote scratch limits at 0 and 24 h. (b) Quantitative Wound Healing: The percentage of wound healing for each group per treatment assessed through histograms: MTX-Lf-SLNs have resulted in the most significant wound closure. Asterisk, p. (c) Hen's Egg Test-Chorioallantoic Membrane (CAM) Assay: Bar graphs of sample images. The negative control used was PBS, while Avastin served as the positive control, which notably suppressed VEGF-induced angiogenesis. MTX demonstrated a moderate inhibition of vessels (~ 75% of the control), while MTX-SLNs enhanced the anti-angiogenic effect (~ 55% of the control), and MTX-Lf-SLNs exhibited the strongest inhibition (~ 25% of the control), indicating that lactoferrin plays a role in interfering with VEGF and improving nanoparticle absorption via the targeted receptor. (d) Quantitative Examination of Angiogenic Metrics: Proportional decrease in vessel length, size, and junctions compared to the control. MTX demonstrated moderate inhibition (~ 25%), while MTX-SLNs resulted in a more significant effect (~ 45%), and MTX-Lf-SLNs caused the most substantial suppression (~ 70%). Analysis with ImageJ validated these results.

augmenting the anti-angiogenic efficacy of MTX through both direct suppression of angiogenesis and enhanced delivery of nanoparticles. MTX-Lf-SLNs showed a greater decrease in wound healing and vascular parameters compared to MTX-SLNs, and this presents a promising approach for cancer therapy targeting angiogenesis. The study further opens the possibility of combining chemotherapy with bioactive carriers such as lactoferrin for achieving optimal therapeutic benefits.

Our study involving the use of the Hen's Egg Test-Chorioallantoic Membrane (CAM) assay to examine the anti-angiogenic activity of methotrexate (MTX), MTX-loaded solid lipid nanoparticles (MTX-SLNs), and lactoferrin-conjugated MTX-Lf-SLNs matches the work of M. Polláková et al.[71], on "spitting" cobra venoms. In their study, the venom caused vasoactivity, including hyperemia and hemorrhage, with Naja nigricollis producing the highest embryonic mortality at 100% within 240 s. Comparatively, our study measured the reductions in vessel coverage. PBS: 100%, Avastin: 35% ± 5%, MTX: 75% ± 4%, MTX-SLNs: 55% ± 3%, and MTX-Lf-SLNs: 25% ± 2%. Both studies validate CAM's utility in analyzing vascular phenomena, thus underlining its importance in both toxicological and therapeutic research.

Discussion

This research shows the outstanding potential of Lactoferrin-conjugated Methotrexate-loaded solid lipid nanoparticles (MTX-Lf-SLNs) as a superior targeted therapeutic approach for colorectal cancer, with improvements in cellular efficacy and biocompatibility compared to conventional Methotrexate (MTX) formulations. The cytotoxicity studies showed a notable increase in the potency of MTX-Lf-SLNs, with an IC50 of 0.51 ± 0.02 μM, exceeding that of MTX-SLNs (1.83 ± 0.3 μM) and free MTX (2.04 ± 0.5 μM). This enhancement is consistent with the receptor-specific uptake mediated by LRP1 receptors overexpressed in cancer cells, which enhances intracellular drug delivery. The size of the nanoparticles is 154.18 ± 8.26 nm, and their enhanced zeta potential is −33.37 ± 4.11 mV, which indicates good colloidal stability and bioavailability, hence suitable for systemic delivery. Controlled drug release studies indicated sustained delivery under acidic tumour-like conditions (70% release at pH 5.7 over 24 h), which significantly reduced systemic toxicity and enhanced therapeutic efficacy. These results are in line with recent Jazmín Torres et al.[72], research, which have demonstrated the surface modification of AuNPs onto liposomes (L)-doxorubicin (Dox) enhances targeted drug delivery to tumour sites. Through this functionalization, there is pH/light-responsive drug release, enhancing the anticancer efficacy by means of photothermal therapy.

Molecular docking and dynamics simulations confirmed the strong, stable binding of MTX to Caspase-6 with a docking score of −9.316 and key interactions with residues like Arg220 and Asp262, pointing out its potential apoptotic mechanism. Complementary apoptosis-inducing assays showed high induction of apoptosis, wherein MTX-Lf-SLNs induced 40.0 ± 3.7% early and 30.0 ± 1.7% late apoptosis compared to MTX and MTX-SLNs, which were significantly better than the latter. This was further supported by DAPI staining, where MTX-Lf-SLNs-treated cells presented most significant nuclear condensation and chromatin fragmentation, affirming its higher potential to induce apoptosis.

Biopharmaceutically, MTX-Lf-SLNs had excellent tumour-targeting capabilities since a 70% decrease in angiogenesis was found to be associated with MTX-Lf-SLNs as compared to PBS controls due to the dual action of cytotoxicity of MTX and VEGF-modulating properties of lactoferrin (Lf). Inhibiting tumour vascularization while preserving cellular targeting is a step forward in anti-cancer strategies and corresponds to recent research demonstrating that bioactive carriers enhance drug efficacy through receptor-mediated pathways and synergistic anti-angiogenic effects. The studies on ROS modulation revealed that free MTX induced oxidative stress, whereas MTX-Lf-SLNs strategically counteracted excessive ROS production, thereby reducing oxidative damage to normal cells and preserving mitochondrial function. This is supported by mitochondrial membrane potential (MMP) assays, showing a red/green fluorescence ratio of 4.4 ± 0.4 for MTX-Lf-SLNs-treated cells, against 2.1 ± 0.2 for free MTX, thus indicating better protection towards mitochondria. Similar types of findings have also been obtained through recent nanoparticle-based therapeutic strategies that balance the pro-apoptotic and protective mechanisms for optimized therapeutic effects. In addition, wound-healing assays showed greater inhibition of cellular migration by MTX-Lf-SLNs (30.23% closure) as compared to MTX-SLNs (53.44%) and free MTX (66.35%), thus showing that they could inhibit metastatic progression.

Mechanistically, the introduction of lactoferrin both increased cellular uptake and improved pharmacokinetic and stability profiles for the nanoparticles as evidenced through encapsulation efficiency (80.11%), drug loading (28.67%), and low drug leakage (< 4.6%) over a period of 3 months. Analysis through FTIR and DSC further proved that encapsulation of MTX occurred within the nanoparticle matrix, which also had the structural integrity provided by lactoferrin along with targeted binding capabilities. These results are in good agreement with previous studies that highlighted the key role of glycoproteins such as lactoferrin in enhancing the functionality of nanoparticles and targeting specificity. In addition, the sum of MTX inhibition via DHFR and lactoferrin receptor-mediated targeting effects led to considerable Caspase-6 activation, which were confirmed by immunofluorescence studies (average fluorescence intensity: 20.2 ± 1.8 RFI of MTX-Lf-SLNs vs. free MTX at 45.6 ± 3.2 RFI). This suggests a dual apoptotic mechanism mediated by mitochondrial dysfunction and caspase activation, offering a strong therapeutic advantage.

The findings highlight MTX-Lf-SLNs as a multifaceted nanotherapeutic platform that bridges pharmacological efficacy, targeted delivery, and reduced systemic toxicity. Nanoparticulate formulations notably decreased TNF-α (17.6 ± 2.1 pg/mL), IL-6 (20.2 ± 1.9 pg/mL), and IL-1β (15.4 ± 3.4 pg/mL), suggesting reduced inflammation and improved biocompatibility. Lowered ICAM-1 and HLA-DR expression further validated diminished immune activation, indicating regulated drug release, limited systemic toxicity, and enhanced pharmacological effectiveness in colon cancer treatment. In addition to amplifying drug bioavailability and receptor specificity, the incorporation of lactoferrin as a bioactive ligand introduces complementary anti-angiogenic and immunomodulatory effects, as evidenced by enhanced anti-tumour response in in-vitro and in-ovo models. These results are consistent with the emerging paradigm of precision nanomedicine, which uses multi-functional nanoparticles to address the complexity of cancer biology. MTX-Lf-SLNs are an important step forward in developing targeted colon cancer therapies and have translational potential for clinical applications. Future studies in in-vivo pharmacokinetics and combination therapies will further establish the utility of this platform in overcoming current therapeutic limitations and advancing personalized oncology.

Conclusions

The study clarifies the significant superiority of Lactoferrin-conjugated Methotrexate-loaded Solid Lipid Nanoparticles (MTX-Lf-SLNs) as a targeted therapeutic drug delivery platform for colorectal cancer. Through comprehensive molecular docking, molecular dynamics, and physicochemical characterization, MTX-Lf-SLNs showed stable binding, controlled release, and enhanced bioavailability. Cellular assays confirmed significant improvements in cytotoxicity, apoptosis induction, and mitochondrial preservation over free MTX and MTX-SLNs. Mechanistically, conjugation of lactoferrin allowed receptor-mediated uptake, enhanced anti-angiogenic

activity, and reduced systemic toxicity. In vitro and in vivo findings collectively demonstrate the MTX-Lf-SLNs potential to overcome conventional chemotherapy limitations by integrating molecular accuracy with biocompatible delivery. Nanoparticulate formulations enhanced biocompatibility, decreased cytokine release, and lowered immune activation, presenting a promising targeted approach for colon cancer therapy. These findings serve as a springboard for moving MTX-Lf-SLNs into clinical use and ushering in a paradigm shift in colorectal cancer management with personalized and less-invasive nanomedicine approaches.

Data availability

The datasets generated and/or analyzed during the current study are not publicly available due to confidentiality and proprietary considerations but are available from the corresponding author upon reasonable request.

Received: 26 February 2025; Accepted: 18 June 2025
Published online: 01 July 2025

References

1. Pallathadka, H. et al. Specific small interfering RNAs (siRNAs) for targeting the metastasis, immune responses, and drug resistance of colorectal cancer cells (CRC). *Int. Immunopharmacol.* **140**, 112730. https://doi.org/10.1016/j.intimp.2024.112730 (2024).
2. Marunaka, Y. et al. Re-examining the optimal extent of lymph node dissection for colon cancer using the lymphadenectomy index. *Sci. Rep.* **15**, 6575. https://doi.org/10.1038/s41598-025-91250-2 (2025).
3. Chandegra, B., Prajapati, P. & Prajapati, B. G. in *Colorectal Cancer* (eds Bhupendra G. Prajapati, Anil K. Philip, & Sankha Bhattacharya) 95–113 (Academic Press, 2024).
4. Aghanejad, A. et al. Targeted co-delivery nanosystem based on methotrexate, curcumin, and PAMAM dendrimer for improvement of the therapeutic efficacy in cervical cancer. *Sci. Rep.* **15**, 1813. https://doi.org/10.1038/s41598-024-82074-7 (2025).
5. Sayed Ahmed, A. M., AbdalSalam, M. H., Zohairy, E. A. F., El-Komy, M. H. M. & Abdelgwad, M. Methotrexate toxicity pattern among Egyptian patients: possible implications of glomerular filtration rate and methotrexate level on low-dose MTX-related toxicities. *Toxicol. Anal. Et Clinique*. https://doi.org/10.1016/j.toxac.2024.10.002 (2024).
6. Hanna, D. H., Hamed, A. A. & Saad, G. R. Synthesis and characterization of Poly(3-hydroxybutyrate)/chitosan-graft Poly (acrylic acid) conjugate hyaluronate for targeted delivery of methotrexate drug to colon cancer cells. *Int. J. Biol. Macromol.* **240**, 124396. https://doi.org/10.1016/j.ijbiomac.2023.124396 (2023).
7. Dabrowska, M., Uram, Ł., Dabrowski, M. & Sikora, E. Antigen presentation capability and AP-1 activation accompany methotrexate-induced colon cancer cell senescence in the context of aberrant β-catenin signaling. *Mech. Ageing Dev.* **197**, 111517. https://doi.org/10.1016/j.mad.2021.111517 (2021).
8. Wang, G. et al. Caspase-8 promotes innate immunity in the Chinese mitten crab by regulating the expression of antimicrobial peptides and apoptosis in hemocyte. *Dev. Comp. Immunol.* 105308. https://doi.org/10.1016/j.dci.2024.105308 (2024).
9. Aly, S., El-Kamel, A. H., Sheta, E. & El-Habashy, S. E. Chondroitin/Lactoferrin-dual functionalized pterostilbene-solid lipid nanoparticles as targeted breast cancer therapy. *Int. J. Pharm.* **642**, 123163. https://doi.org/10.1016/j.ijpharm.2023.123163 (2023).
10. Zarbab, A., Sajjad, A., Rasul, A., Jabeen, F. & Javaid Iqbal, M. Synthesis and characterization of Guar gum based biopolymeric hydrogels as carrier materials for controlled delivery of methotrexate to treat colon cancer. *Saudi J. Biol. Sci.* **30**, 103731. https://doi.org/10.1016/j.sjbs.2023.103731 (2023).
11. Dadashi, H. et al. Enhancing ovarian cancer treatment: synergistic effects of methotrexate (Methotrexate)- and quercetin-loaded Chitosan nanoparticles. *Carbohydr. Polym. Technol. Appl.* **8**, 100619. https://doi.org/10.1016/j.carpta.2024.100619 (2024).
12. Barroso, N. G. et al. β-carotene and Resveratrol loaded glycerol monostearate-based oleogels: physicochemical characterization at low gelation concentrations. *Food Res. Int.* **197**, 115181. https://doi.org/10.1016/j.foodres.2024.115181 (2024).
13. Wan, H., Sun, D. W., Zhu, Z. & Zeng, L. Fabrication and characterization of biomimetic plant cuticles from pullulan - graphene oxide (PU-GO) and beeswax - stearic acid (BW-SA) for Citrus Limon Rosso preservation. *Int. J. Biol. Macromol.* **254**, 127776. https://doi.org/10.1016/j.ijbiomac.2023.127776 (2024).
14. Wróbel, M. et al. Vitamin d-binding protein (VDBP) and lactoferrin (LF) in plasma and peritoneal fluid (PF) in the diagnosis of endometriosis. *Eur. J. Obstet. Gynecol. Reprod. Biol.* **293**, 54. https://doi.org/10.1016/j.ejogrb.2023.08.163 (2024).
15. Khatibi, Z., Kazemi, N. M. & Khaleghi, S. Targeted and biocompatible NMOF as efficient nanocomposite for delivery of methotrexate to colon cancer cells. *J. Drug Deliv. Sci. Technol.* **73**, 103441. https://doi.org/10.1016/j.jddst.2022.103441 (2022).
16. Zhang, G. et al. Regulation of NLRP3 inflammasome and Caspase-3/4/11 by 2′,4′-dihydroxychalcone contributes to anti-colorectal cancer. *Phytomedicine* **135**, 156194. https://doi.org/10.1016/j.phymed.2024.156194 (2024).
17. Khan, S. & Khatri, D. K. In-silico screening to identify phytochemical inhibitor for hP2X7: A crucial inflammatory cell death mediator in Parkinson's disease. *Comput. Biol. Chem.* **115**, 108285. https://doi.org/10.1016/j.compbiolchem.2024.108285 (2025).
18. Anjum, S. M. et al. Identification of a natural antagonist for signal transducer and activator of transcription 3 (STAT3) by computational approach. *Results Chem.* **5**, 100970. https://doi.org/10.1016/j.rechem.2023.100970 (2023).
19. Mishra, N. et al. Transporter targeted-carnitine modified pectin-chitosan nanoparticles for inositol hexaphosphate delivery to the colon: an in Silico and in vitro approach. *Int. J. Biol. Macromol.* **263**, 130517. https://doi.org/10.1016/j.ijbiomac.2024.130517 (2024).
20. Razali, R. H., Teh, L. K., Salleh, M. Z., Teh, K. H. & Mohd Ibrahim, H. Differential metabolomic pathway analysis in Malaysian childhood acute lymphoblastic leukemia patients treated with high-dose methotrexate. *Pediatr. Hematol. Oncol. J.* **9**, 193–199. https://doi.org/10.1016/j.phoj.2024.06.004 (2024).
21. Bello, M. & Rodríguez-Fonseca, R. A. Complexation of methotrexate via ligand diffusion molecular dynamic simulations under neutral, basic, and acidic conditions. *J. Mol. Graph. Model.* **93**, 107443. https://doi.org/10.1016/j.jmgm.2019.107443 (2019).
22. Kagami, L. P., das Neves, G. M., Timmers, L. F. S. M., Caceres, R. A. & Eifler-Lima, V. L. Geo-Measures: A PyMOL plugin for protein structure ensembles analysis. *Comput. Biol. Chem.* **87**, 107322. https://doi.org/10.1016/j.compbiolchem.2020.107322 (2020).
23. Krishnasailaja, A. & Gazi, A. S. Formulation of methotrexate loaded solid lipid nanoparticles by Micro emulsion technique. *Curr. Nanomater.* **8**, 153–161. https://doi.org/10.2174/2405461507666220428121823 (2023).
24. Shinde, M. et al. Unleashing potential of methotrexate-amino acid Methyl ester-loaded lipidic nanocapsules as magic bullets against resistant breast cancer. *J. Drug Deliv. Sci. Technol.* **104**, 106539. https://doi.org/10.1016/j.jddst.2024.106539 (2025).
25. Kuo, Y. C. & Cheng, S. J. Brain targeted delivery of carmustine using solid lipid nanoparticles modified with Tamoxifen and lactoferrin for antitumor proliferation. *Int. J. Pharm.* **499**, 10–19. https://doi.org/10.1016/j.ijpharm.2015.12.054 (2016).
26. Liu, F. et al. Novel succinimide-based ionic liquids as efficient and sustainable media for methanolysis of polycarbonate to recover bisphenol A (BPA) under mild conditions. *Polym. Degrad. Stab.* **169**, 108996. https://doi.org/10.1016/j.polymdegradstab.2019.108996 (2019).

27. Kumar, V., Kumar, N., Gangwar, A. K. & Singh, H. Comparison of acellular small intestinal matrix (ASIM) and 1-ethyl-3-(3-dimethylaminopropyl)carbodiimide crosslinked ASIM (ASIM-EDC) for repair of full-thickness skin wounds in rabbits. *Wound Med.* **7**, 24–33. https://doi.org/10.1016/j.wndm.2015.01.001 (2014).
28. Tekko, I. A. et al. Development and characterisation of novel Poly (vinyl alcohol)/poly (vinyl pyrrolidone)-based hydrogel-forming microneedle arrays for enhanced and sustained transdermal delivery of methotrexate. *Int. J. Pharm.* **586**, 119580. https://doi.org/10.1016/j.ijpharm.2020.119580 (2020).
29. Suenaga, S. et al. How does the powder mixture of ibuprofen and caffeine attenuate the solubility of ibuprofen? Comparative study for the Xanthine derivatives to recognize their intermolecular interactions using Fourier-Transform infrared (FTIR) spectra, differential scanning calorimetry (DSC), and X–ray powder diffractometry (XRPD). *Mol. Pharm.* https://doi.org/10.1021/acs.molpharmaceut.4c00429 (2024).
30. Sahin, I. Cholecalciferol has strong effect on the order and dynamics of DPPC membranes: A combined fourier transform infrared spectroscopy and differential scanning calorimetry study. *Vib. Spectrosc.* **113**, 103207. https://doi.org/10.1016/j.vibspec.2021.103207 (2021).
31. Dehury, P., Chaudhari, S., Banerjee, T. & Kumar Das, S. Prediction of thermophysical properties of deep eutectic solvent-based organic nanofluids: A machine learning approach. *J. Mol. Liq.* **411**, 125809. https://doi.org/10.1016/j.molliq.2024.125809 (2024).
32. Cyriac, J., Thomas, B., Sreejit, C. M., Yuvaraj, M. & Joseph, S. Chitosan zinc nanocomposite: A promising slow releasing zinc nano fertilizer. *Mater. Today: Proc.* https://doi.org/10.1016/j.matpr.2023.11.062 (2023).
33. Pradheepa, R., Manimehan, I. & Sakthivel, P. Structural, bandgap tailoring, photoluminescence and electrochemical characteristics of Sm3+-doped ZnS quantum Dots prepared in Ar-atmosphere. *Mater. Sci. Eng.: B* **306**, 117463. https://doi.org/10.1016/j.mseb.2024.117463 (2024).
34. Tynkevych, O., Ryczek, K., Kuciel, T. & Zaraska, L. Formation of ZrO2 with unusual morphology and Zr surface patterning via one-step anodization of zirconium in aqueous electrolyte. *J. Mater. Res. Technol.* **34**, 100–109. https://doi.org/10.1016/j.jmrt.2024.12.045 (2025).
35. Yuniarti, N. & Yulizar, Y. Chitosan nanoparticles modified by Anredera cordifolia (Ten.) steenis leaf extract for enhancement of Azithromycin encapsulation efficiency and loading capacity: in vitro drug release study. *J. Pharm. Sci.* **112**, 3164–3174. https://doi.org/10.1016/j.xphs.2023.07.021 (2023).
36. Sun, Y. et al. Preparation and characterization of lactoferrin-polyphenol conjugate with stabilizing effects on fish oil high internal phase Pickering emulsions. *Food Chem.: X* **24**, 101836. https://doi.org/10.1016/j.fochx.2024.101836 (2024).
37. Valappil, S. P. et al. Novel lactoferrin-conjugated gallium complex to treat Pseudomonas aeruginosa wound infection. *Int. J. Biol. Macromol.* **258**, 128838. https://doi.org/10.1016/j.ijbiomac.2023.128838 (2024).
38. Mittal, S. et al. Quality by design engineered, enhanced anticancer activity of Temozolomide and Resveratrol coloaded NLC and brain targeting via lactoferrin conjugation in treatment of glioblastoma. *Eur. J. Pharm. Biopharm.* **191**, 175–188. https://doi.org/10.1016/j.ejpb.2023.08.018 (2023).
39. Vaidya, R., Ren, E. J., Shi, T., Gardia, A. & Ren, W. A slow and sustained release of methotrexate (MTX) from a new polymeric dicalcium phosphate dehydrate cement (P-DCPD). *Mater. Adv.* **2**, 4652–4658. https://doi.org/10.1039/d1ma00188d (2021).
40. Kasif, M. et al. Development of biocompatible lipid-polymer hybrid nanoparticles for enhanced oral absorption of posaconazole: A mechanistic in vitro and in Silico assessment. *J. Drug Deliv. Sci. Technol.* **101**, 106109. https://doi.org/10.1016/j.jddst.2024.106109 (2024).
41. Shao, M. et al. Expediting the development of robust 5-FU-resistant colorectal cancer models using innovative combined in vivo and in vitro strategies. *Biomed. Pharmacother.* **180**, 117576. https://doi.org/10.1016/j.biopha.2024.117576 (2024).
42. Shao, W. et al. Hyaluronic acid-conjugated methotrexate and 5-fluorouracil for targeted drug delivery. *Int. J. Biol. Macromol.* **273**, 132671. https://doi.org/10.1016/j.ijbiomac.2024.132671 (2024).
43. Mohite, P. et al. Nanoemulsion in management of colorectal cancer: challenges and future prospects. *Nanomanufacturing* **3**, 139–166 (2023).
44. Frouin, I. et al. Different effects of methotrexate on DNA mismatch repair proficient and deficient cells. *Eur. J. Cancer.* **37**, 1173–1180. https://doi.org/10.1016/S0959-8049(01)00095-8 (2001).
45. Hu, Y. et al. Bismuth oxide nanoparticles inhibit HCT116 colorectal cancer cells by inducing apoptosis, cell cycle arrest and ROS production. *Process Biochem.* **148**, 124–138. https://doi.org/10.1016/j.procbio.2024.11.017 (2025).
46. Kaimuangpak, K., Rosalina, R., Thumanu, K. & Weerapreeyakul, N. Macromolecules with predominant β-pleated sheet proteins in extracellular vesicles released from Raphanus sativus L. Var. Caudatus Alef microgreens induce DNA damage-mediated apoptosis in HCT116 colon cancer cells. *Int. J. Biol. Macromol.* **269**, 132001. https://doi.org/10.1016/j.ijbiomac.2024.132001 (2024).
47. Ashwanikumar, N., Kumar, N. A., Nair, S. A. & Kumar, G. S. V. Dual drug delivery of 5-fluorouracil (5-FU) and methotrexate (MTX) through random copolymeric nanomicelles of PLGA and polyethylenimine demonstrating enhanced cell uptake and cytotoxicity. *Colloids Surf., B.* **122**, 520–528. https://doi.org/10.1016/j.colsurfb.2014.07.024 (2014).
48. Tang, J. L. Y. et al. A methotrexate labelled dual metal oxide nanocomposite for long-lasting anti-cancer theranostics. *Mater. Today Bio.* **30**, 101377. https://doi.org/10.1016/j.mtbio.2024.101377 (2025).
49. Kundrapu, D. B., Rao, P. A. & Malla, R. R. Enhanced efficacy of Quercetin and taxifolin encapsulated with pH-responsive injectable BSA hydrogel for targeting triple-negative breast cancer cells. *Int. J. Biol. Macromol.* **287**, 138477. https://doi.org/10.1016/j.ijbiomac.2024.138477 (2025).
50. Yu, M., Li, Q. & Yu, H. Characterization of cellular uptake, anti-colorectal cancer effects and pharmacokinetics of curcumin-loaded polypropylene/rice husk composites filled with nano-SiO2. *Alexandria Eng. J.* **101**, 118–124. https://doi.org/10.1016/j.aej.2024.05.074 (2024).
51. Fernández-Villa, D. et al. Design of tunable hyaluronic acid and O′-carboxymethyl Chitosan formulations for the minimally invasive delivery of multifunctional therapies targeting rheumatoid arthritis. *Carbohydr. Polym.* **349**, 123018. https://doi.org/10.1016/j.carbpol.2024.123018 (2025).
52. Amaldoss, M. J. N. et al. Detection and quantification of nanoparticle-induced intracellular ROS in live cells by laser scanning confocal microscopy. *Methods* **207**, 11–19. https://doi.org/10.1016/j.ymeth.2022.08.005 (2022).
53. Mohanty, S., Panda, S., Devadharshini, U. & Paul, S. Proteins and their functionalization for finding therapeutic avenues in cancer: current status and future prospective. *Biochim. Et Biophys. Acta (BBA) - Reviews Cancer*. **1878**, 188862. https://doi.org/10.1016/j.bbcan.2023.188862 (2023).
54. Tarawneh, N. et al. Downregulation of Aquaporins and PI3K/AKT and upregulation of PTEN expression induced by the flavone scutellarein in human colon cancer cell lines. *Heliyon* **10**, e39402. https://doi.org/10.1016/j.heliyon.2024.e39402 (2024).
55. Mao, K. et al. Integrated network Pharmacology and transcriptomic approach reveal the role of equol in reducing colorectal cancer via regulating multiple cell cycle genes in HCT116 cells. *Int. J. Biol. Macromol.* **282**, 136832. https://doi.org/10.1016/j.ijbiomac.2024.136832 (2024).
56. Fernandes, A. S. et al. Pedunculagin and tellimagrandin-I stimulate inflammation and angiogenesis and upregulate vascular endothelial growth factor and tumor necrosis factor-alpha in vivo. *Microvasc. Res.* **151**, 104615. https://doi.org/10.1016/j.mvr.2023.104615 (2024).
57. Li, W. et al. Triptolide and methotrexate binding competitively to bovine serum albumin: A study of spectroscopic experiments, molecular docking, and molecular dynamic simulation. *J. Mol. Liq.* **367**, 120300. https://doi.org/10.1016/j.molliq.2022.120300 (2022).

58. Xu, F. et al. Increase delivery, cytotoxicity, stability and induction of apoptosis in cisplatin by Establishing a new complex with methotrexate. *J. Drug Deliv. Sci. Technol.* **86**, 104683. https://doi.org/10.1016/j.jddst.2023.104683 (2023).
59. Shah, R. & Bhattacharya, S. Preparation and physical characterization of methotrexate encapsulated Poly (n-methyl glycine) microspheres for the rheumatoid arthritis treatment option. *Results Chem.* **5**, 100875. https://doi.org/10.1016/j.rechem.2023.100875 (2023).
60. Barkat, M. A. et al. Formulation development of methotrexate lipid-based nanogel for treatment of skin cancer. *Colloids Surf., A.* **688**, 133571. https://doi.org/10.1016/j.colsurfa.2024.133571 (2024).
61. Danafar, H. et al. Co-delivery of methotrexate and Curcumin with mPEG-PCL polymeric nanoparticles and evaluation of toxicity effect on MCF7 breast cancer cell line. *Inorg. Chem. Commun.* **142**, 109715. https://doi.org/10.1016/j.inoche.2022.109715 (2022).
62. Maiti, D. et al. Evaluation of solid-lipid nanoparticles formulation of methotrexate for anti-psoriatic activity. *Saudi Pharm. J.* **31**, 834–844. https://doi.org/10.1016/j.jsps.2023.04.007 (2023).
63. Raval, H. et al. Fabrication of lactoferrin-chitosan-etoposide nanoparticles with melatonin via carbodiimide coupling: In-vitro & in-vivo evaluation for colon cancer. *J. Controlled Release*. **377**, 810–841. https://doi.org/10.1016/j.jconrel.2024.11.077 (2025).
64. dos Santos, A. M. et al. 5-Fluorouracil-loaded Chitosan nanoparticles conjugated with methotrexate for targeted therapy of colorectal cancer. *Int. J. Biol. Macromol.* **287**, 138342. https://doi.org/10.1016/j.ijbiomac.2024.138342 (2025).
65. Huang, W. Y., Yang, P. M., Chang, Y. F., Marquez, V. E. & Chen, C. C. Methotrexate induces apoptosis through p53/p21-dependent pathway and increases E-cadherin expression through downregulation of HDAC/EZH2. *Biochem. Pharmacol.* **81**, 510–517. https://doi.org/10.1016/j.bcp.2010.11.014 (2011).
66. Ayed-Boussema, I., Rjiba-Touati, K., Hamdi, H., Chaabani, H. & Abid-Essefi, S. Oxidative stress-mediated mitochondrial apoptosis induced by the acaricide, fenpyroximate, on cultured human colon cancer HCT 116 cells. *Toxicol. In Vitro*. **89**, 105587. https://doi.org/10.1016/j.tiv.2023.105587 (2023).
67. Algandaby, M. M. & Al-Sawahli, M. M. Augmentation of anti-proliferative, pro-apoptotic and oxidant profiles induced by Piceatannol in human breast carcinoma MCF-7 cells using Zein nanostructures. *Biomed. Pharmacother.* **138**, 111409. https://doi.org/10.1016/j.biopha.2021.111409 (2021).
68. Chen, Y. et al. Targeting ferroptosis with polymerized platinum (IV) prodrugs nanoparticles with everolimus for enhancing therapeutic efficacy on cholangiocarcinoma. *Nano Today*. **59**, 102531. https://doi.org/10.1016/j.nantod.2024.102531 (2024).
69. Secme, M., Mutlu, D., Elmas, L. & Arslan, S. Assessing effects of caffeic acid on cytotoxicity, apoptosis, invasion, GST enzyme activity, oxidant, antioxidant status and micro-RNA expressions in HCT116 colorectal cancer cells. *South. Afr. J. Bot.* **157**, 19–26. https://doi.org/10.1016/j.sajb.2023.03.046 (2023).
70. Bhattacharya, S., Raval, H. & Bhirud, D. Hyaluronic acid-functionalized carboxymethyl dextran-coated melatonin nanoconjugates for targeted Etoposide delivery in metastatic colon cancer: extensive in-vitro investigation in HCT116 cell lines, antimicrobial efficacy, and anti-angiogenic potential in chick Chorioallantoic membrane (CAM) assay. *Int. J. Biol. Macromol.* **281**, 136373. https://doi.org/10.1016/j.ijbiomac.2024.136373 (2024).
71. Polláková, M. et al. Spitting cobras: experimental assay employing the model of chicken embryo and the chick Chorioallantoic membrane for imaging and evaluation of effects of venom from African and Asian species (Naja ashei, Naja nigricollis, Naja siamensis, Naja sumatrana). *Toxicon* **189**, 79–90. https://doi.org/10.1016/j.toxicon.2020.10.025 (2021).
72. Torres, J. et al. A quality-by-design approach for optimizing the functionalization of gold nanoparticles onto the surface of doxorubicin-encapsulated liposomes. *Int. J. Pharm.* **669**, 125040. https://doi.org/10.1016/j.ijpharm.2024.125040 (2025).

Acknowledgements
This project could not have been achieved without the assistance and backing of Dr. R.S. Gaud, Advisor to the Chancellor, SVKM's NMIMS Deemed-to-be University, Mumbai, India. The authors also wish to express their gratitude to DIYA LAB, Mumbai, India, for offering logistical and analytical support during the project's development. Furthermore, the authors express their appreciation to Aakaar Biotechnologies Private Limited, Lucknow, Uttar Pradesh, and the Chemical Biology Unit at the Institute of Nano Science and Technology (INST), India, for carrying out the in-vitro anticancer activity.

Author contributions
Sankha Bhattacharya: Development of the concept, data validation, oversight, composing the primary manuscript, visual representation, securing funding, and correspondence with the journal in the role of corresponding author. Ranajit Nivrutti Shinde, Vishal Beldar, Satyam Sharma, Rehan Khan: were involved in the conceptualization, validation, and writing of the initial draft. Every author examined and consented to the final version of the manuscript.

Funding
This study did not obtain any funding from public, commercial, or nonprofit organizations.

Declarations

Competing interests
The authors declare no competing interests.

Additional information
Correspondence and requests for materials should be addressed to S.B.

Reprints and permissions information is available at www.nature.com/reprints.

Publisher's note Springer Nature remains neutral with regard to jurisdictional claims in published maps and institutional affiliations.